This document is downloaded from DR-NTU (https://dr.ntu.edu.sg)
Nanyang Technological University, Singapore.

Synergistic gating of electro-iono-photoactive 2D chalcogenide neuristors : coexistence of Hebbian and homeostatic synaptic metaplasticity

John, Rohit Abharam; Liu, Fucai; Chien, Nguyen Anh; Kulkarni, Mohit Rameshchandra; Zhu, Chao; Fu, Qundong; Basu, Arindam; Liu, Zheng

2018

John, R. A., Liu, F., Chien, N. A., Kulkarni, M. R., Zhu, C., Fu, Q., . . . Mathews, N. (2018). Synergistic gating of electro-iono-photoactive 2D chalcogenide neuristors : coexistence of Hebbian and homeostatic synaptic metaplasticity. Advanced Materials, 30(25), 1800220-. doi:10.1002/adma.201800220

https://hdl.handle.net/10356/138300

https://doi.org/10.1002/adma.201800220

© 2018 WILEY-VCH Verlag GmbH & Co. KGaA, Weinheim. All rights reserved. This paper was published in Advanced Materials and is made available with permission of WILEY-VCH Verlag GmbH & Co. KGaA, Weinheim.

Downloaded on 27 Aug 2022 14:07:36 SGT

Synergistic Gating of Electro-Iono-Photoactive 2D Chalcogenide Neuristors: co-existence of Hebbian and Homeostatic Synaptic Metaplasticity

Rohit Abraham John[1]†, *Fucai Liu*[1]†, *Nguyen Anh Chien*[1], *Mohit R. Kulkarni*[1], *Chao Zhu*[1], *Qundong Fu*[1], *Arindam Basu*[2], *Zheng Liu*[1], *Nripan Mathews*[1,3]*

[1] School of Materials Science and Engineering, Nanyang Technological University, 50 Nanyang Avenue, Singapore 639798

[2] School of Electrical and Electronic Engineering, Nanyang Technological University, 50 Nanyang Avenue, Singapore 639798

[3] Energy Research Institute @ NTU (ERI@N), Nanyang Technological University, Singapore 637553

†These authors contributed equally in this work

* Corresponding author

Prof. Nripan Mathews (Email: Nripan@ntu.edu.sg)

Keywords: 2D chalcogenides, Neuromorphic Computing, Hebbian Synaptic Plasticity, Homeostatic regulation, Associative learning

Abstract.

Emulation of brain-like signal processing with thin-film devices could lay the foundation for building artificially intelligent learning circuitry in future. Encompassing higher functionalities into single artificial neural elements will allow the development of robust neuromorphic circuitry emulating biological adaptation mechanisms with drastically lesser neural elements, mitigating strict process challenges and high circuit density requirements necessary to match the computational complexity of the human brain. Here, 2D transition metal di-chalcogenide (TMDC) (MoS_2) neuristors are designed to mimic intracellular ion endocytosis-exocytosis dynamics / neurotransmitter-release in chemical synapses using three approaches: (i) electronic-mode: a defect modulation approach where the traps at the semiconductor-dielectric interface are perturbed, (ii) ionotronic-mode: where electronic responses are modulated via ionic gating and (iii) photoactive-mode: harnessing persistent photoconductivity or trap-assisted slow recombination mechanisms. Exploiting a novel multi-gated architecture incorporating electrical and optical biases, this incarnation not only addresses different charge-trapping probabilities to finely modulate the synaptic weights, but also amalgamates neuromodulation schemes to achieve “plasticity of plasticity-metaplasticity” via dynamic control of Hebbian spike-time dependent plasticity and homeostatic regulation. Co-existence of such multiple forms of synaptic plasticity increases the efficacy of memory storage and processing capacity of artificial neuristors, enabling design of highly efficient novel neural architectures.

In contrast to the conventional serial processing achieved with today's von Neumann architectures, human brain utilizes highly parallel, event-driven, and energy-efficient architectures to achieve computational power of the order of 10^{18} FLOPS at a power consumption of ~ 20 W.[1] With ~ 86 billion neurons in synaptic communication making 10 quadrillion calculations every second, our brain possesses an unmatched parallel processing power with 17.2 trillion action potentials per second.[2] Learning in the brain happens through modification of synaptic weights through processes such as long-term potentiation and depression.[3] Typical cortical neurons have one to ten thousand synaptic connections which operate by electro-chemical signalling using neurotransmitters. For optimum firing, the neuronal dynamics maintains a balanced excitatory status quo via an integration/summation process combined with a mechanism that triggers action potentials above a threshold voltage, as per the leaky Integrate-And-Fire Model.[4] To mimic these neuronal dynamics; conductance change (synaptic weight) of the artificial synaptic circuits has to be tuned continuously to demonstrate plasticity and non-volatility.[5] Mimicking synaptic signal transmission through nanoelectronic circuits thus becomes the cardinal research target in the field of neuromorphic engineering. However, hardware implementation of neural networks emulating synaptic functionalities with comparable complexity and feasible power dissipation remain exceptionally challenging. Neuromorphic circuitry based on conventional Silicon-CMOS technology using memory to store synaptic weights require additional clock cycles to update the weights, thereby imposing issues with power consumption and scalability.[6] Memristors[7,8] with programmable resistance states which are presently in focus, are compromised by excessive write-noise nonlinearities and abrupt conductance transitions which limit the programmable states (and hence accessible synaptic weights). From a technological perspective, highly stringent process requirements and device integrity expectations further worsens the challenge of fabricating high-density circuitry necessary to match the degree of complexity and number of neurons in the human brain.[9–11] An alternative strategy to this would be to incorporate augmentative functionalities into a single neural element to enhance the achievable plasticity and parallelism. This would allow the development of robust neuromorphic circuitry emulating biological adaptation mechanisms with drastically lesser neural elements, mitigating strict process and density requirements. With an additional gate-control, thin-film transistors (TFTs) based on organic[12,13] and inorganic semiconductors[14–16] seems promising in this regard, exploiting hysteresis to achieve dynamic, linear plasticity when compared to abrupt state transitions in a memristor. The degree of such trapping and electrostatic doping-dedoping can be maximized with ultra-thin semiconducting channels encompassing intimate ionic/electronic coupling at the semiconductor-dielectric interface. Additionally, optical control of synaptic weights can help unlock novel neural network architectures with global connectivity, overcoming interconnect limitations, mitigating thermal loss and improving the signal-to-noise ratio. This calls for the need of atomically-thin semiconducting channels with opto-electronically modulatable carrier concentration, and synergistic gating strategies to probe various trapping probabilities and hence the memresistance states in these semiconductors.

2D transition metal di-chalcogenides (TMDCs) with their ultrafast charge carrier dynamics[17,18] and atomic scalability[19] present a platform with highly modulatable optoelectronic transitions[20,21] that could overcome the limitations of previously investigated material classes. Here, we investigate optoelectronic synaptic plasticity in MoS_2 three-terminal devices via three gating approaches and synergistic combinations there-of. Different trapping probabilities are addressed via individual/combined gating techniques, tuning synaptic weights with higher modulability and homeostatic stability. Initial training sequences created short-term changes in the device conductance/weights, which consolidated to long-term plasticity with persistent instructions. Controlled facilitation/depression was achieved through the multi-gated architecture, with the three modes operating additive/subtractive to each other. Additive operation strengthened the degree of weight plasticity, while subtractive operation regulated these weight changes through a negative feedback mechanism called homeostatic plasticity. Co-existence of Hebbian and homeostatic plasticity not only helped prevent runaway excitation during elevated excitability, but also increased synaptic gain and impeded unnecessary synapse silencing during chronic activity suppression[22], enabling design of highly efficient novel neural architectures. Finally, a classical-conditioning experiment (Pavlov's dog) is realized utilizing concurrent optoelectronic activation, demonstrating a basic form of associative-memory in our systems. These comprehensive results benchmark the possible gating approaches required to achieve parallelism and open up new possibilities of multi-gated neural architectures with 2D chalcogenides as a viable material platform.

Results:

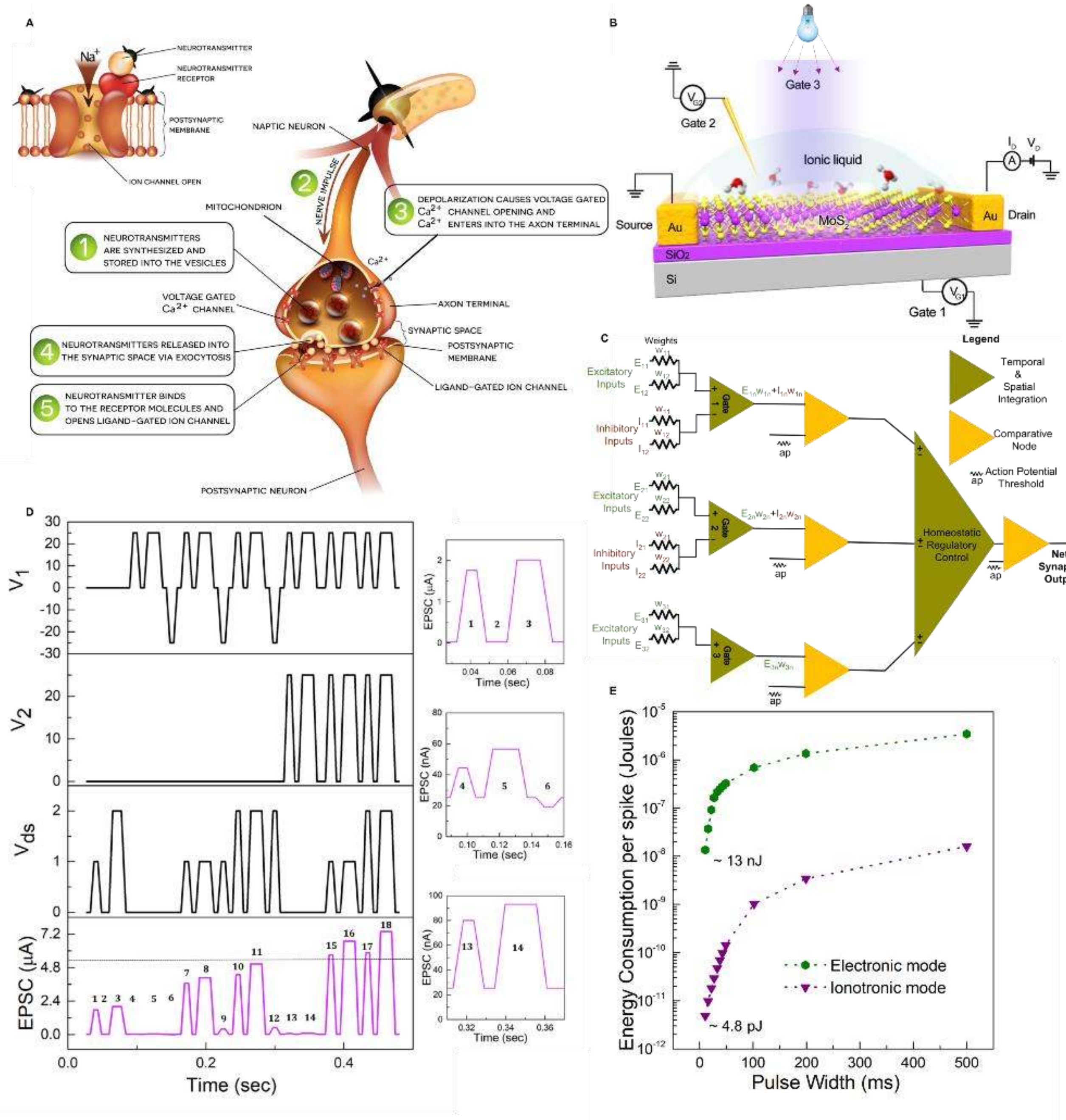

Figure 1. Mimicking synaptic transmission using MoS_2 neuristors. (**A**) Schematic of biological synaptic transmission. (**B**) The proposed multi-gated architecture of analogous artificial MoS_2 synapses. (**C**) Analog circuit depicting interplay between Hebbian and Homeostatic synaptic plasticity. (**D**) Dendritic integration based spiking logic response driven by two presynaptic driving inputs V_1 and V_2, and a modulatory input V_{ds}. Images on the right side represent magnified views of high impedance resistance states. The dotted line represents the threshold current level (5.5 μA) defining logic states "1" and "0". (**E**) Comparison of the ON-state energy consumption per spike (*Eon*) of the MoS_2 synapses as a function of presynaptic pulse width in the electronic and ionotronic-modes. *Eon* was calculated from the equation[23] $E_{on} = I_{peak} \times t \times V$; where I_{peak} is the maximum value of generated EPSC, t is the spike duration, and V is the applied drain voltage. Further scaling down of device dimensions and reducing spike durations to sub-millisecond levels could be utilized as strategies to bring down the energy consumption per event.

MoS_2 Neuristor/Neural-element Configuration. Figure 1A-C illustrates the steps in biological synaptic transmission, the proposed multi-gate device architecture and an analog circuitry depicting interplay between Hebbian and Homeostatic synaptic plasticity respectively. Devices operating in electronic-mode utilised a bottom-gate top-contact configuration with SiO_2 as the dielectric, while ionotronic-mode was enabled by an ionic liquid [N, N-diethyl-N-(2-methoxyethyl)-N-methylammoniumbis-(trifluoromethylsulfonyl)-imide(DEMETFSI)] contact. Device fabrication and physical characterizations are described in detail in the methods section and Supporting-Information Note-1 Figure S1. Both modes exhibited typical n-type depletion-operation with electronic-mode depicting a linear mobility of 28 $cm^2V^{-1}s^{-1}$ when compared to 14.6 $cm^2V^{-1}s^{-1}$ for ionotronic-mode. Interestingly, while devices in the electronic-mode depicted a distinct clockwise hysteresis window of 8 V indicating trapping and detrapping of electrons in the forward and reverse voltage scans[24]; ionotronic-mode operation exhibited an anticlockwise hysteresis window of 0.5 V signifying ion-related electric-double-layer (EDL) modulation in the system[25] (Supporting-Information Note-2 Figure S2). Different trapping possibilities were utilised in both configurations to mimic the ion flux and neurotransmitter release dynamics in chemical synapses. The synaptic transmission steps illustrated in figure 1A is explained in detail in Supporting-Information Note-3. For the synaptic three-terminal devices, gate terminal served as the presynaptic input while the semiconducting 2D TMDC channel with source/drain electrodes were furnished as post-synaptic output terminals. Interfacial traps (electronic-mode) / ions in the ionic liquid (ionotronic-mode) mimicked neurotransmitters, while channel conductance served as the synaptic weight.

To demonstrate comprehensive emulation of synaptic signatures and mimic the essential features of neurotransmitter release, namely- excitatory or inhibitory[26], quantal[27] and probabilistic[28], post-synaptic responses (I_{ds}) triggered by pre-synaptic pulses (V_g) were recorded as a function of pre- and post-synaptic pulse width, pulse interval, frequency and number of repetitions. A combination of these three emulated the cellular machinery responsible for short- and long-term synaptic plasticity. Chemical synapses via expression of facilitation and depression mechanisms, create short and long-term plastic changes within neurons according to the dual-process theory of plasticity.[29] As explained in Supporting-Information Note-3, arrival of an action potential depolarizes the synaptic membrane, causing influx of Ca^{2+} into the presynaptic membrane. When triggered immediately by a temporally correlated action potential, residual Ca^{2+} concentration from the first pulse augments the Ca^{2+} activated by the second pulse, thereby increasing the vesicular release probability and resulting in facilitation. This phenomenon called **Neural Facilitation / Paired-pulse facilitation (PPF)**[30] was emulated by evoking **excitatory post synaptic currents (EPSCs)**[31] in response to paired presynaptic spikes as shown in Supporting-Information Note-4 Figure S3, Table T1. Small pulse intervals (< 30 ms) triggered EPSCs with higher strength when compared to the priori spikes resulting in a strong facilitation index >> 100%. Slower ion relaxation kinetics in the ionotronic-mode enhanced this facilitation index depicting a higher ratio of ~206% when compared to 165% for the electronic-mode. Larger pulse intervals weakened this augmentation with the PPF index reaching around 100 % for a pulse interval of 500 ms. Such temporal enhancement of synaptic connections mimicked the excitatory nature of neurotransmitter release[26,32], analogous to glutamatergic systems, resulting in **short-term potentiation (STP).**[33] Similar activation by inhibitory presynaptic spikes resulted in **short-term depression (STD)** (Supporting-Information Note-4 Figure S3). In the electronic-mode, the spiking rise and decay in EPSCs was caused by electron trapping-detrapping at the semiconducting channel, while ion migration-relaxation kinetics at the ionic liquid-semiconductor interface (Helmholtz double layer) accounted for this phenomena in the ionotronic-mode. For PPF in the electronic/ionotronic-mode, when the pulse interval was shorter than relaxation time of trapped electrons/mobile cations, some of these trapped electrons/ions were unable to return to their equilibrium positions before the second spike was initiated. As a result, these residual electrons/cations induced additional charges in the channel, leading to an increase in channel current and higher PPF index. Large pulse interval allowed these mobile electrons/cations to relax back to their equilibrium positions prior to the second spike application leading to weak channel current modulation and lower PPF index.[16]

Extending the STP behaviour, **quantal release**[27] of neurotransmitters in a chemical synapse was captured as post-synaptic weight changes in response to frequency dependent action potentials. **Dynamic frequency dependent filters**[34] established causal relations between neighbouring neurons, with specific temporal patterns of activity in neural network. Both electronic and ionotronic-modes exhibited high frequency facilitation characteristics analogous to synapses with low initial probability of vesicle release. Similarly, short-term synaptic depression could be represented by low-pass temporal filters.[35] These were in turn integrated with an external microcontroller circuitry and a photoresistor for obstacle detection as explained in (Supporting-Information Note-4 figure S4). An obstacle proximity of < 2 cm caused conductance changes to the photoresistor, in turn triggering presynaptic firing rate at 45 Hz via a processing circuit, resulting in temporal neural spiking activity with a gain of 1.86 and 16.51 for the electronic and ionotronic-modes respectively (figure S4-B, C). The quantal neurotransmitter release model assumes finite number of neurotransmitters per synaptic vesicle, where the final EPSC is the sum of activated miniature EPSCs. Increment in EPSCs as a function of presynaptic pulses number modelled the increase in neurotransmitter release and strengthening of synaptic connections with higher number of action potentials. The obtained learning curves followed an exponential growth behaviour as postulated by Ebbinghaus (Supporting-Information Note-4 figure S5) and depicted a progressive enforcement of synaptic activity, related to learning process and memory recall.[36]

Dendritic Integration. In a neuron, spatiotemporal summation of action potentials triggers a singular change in membrane potential, as per the "integrate and fire neuron model".[37,38] Here, we utilize multiple presynaptic gate inputs (two driving inputs V_1 and V_2 and one modulatory input (V_d/V_{ds}), to demonstrate a neuronal arithmetic with **dynamic spiking logic** "OR" and "AND" operations in the electronic-mode, akin to dendritic integration in neurons (Figure 1D). Logic states

1 to 3 represented strong modulation of post-synaptic responses as a function of the modulatory input V_{ds}. This also accounted for the multiplicative neural logic depicted in figure S6-A. Asynchronous firing or absence of any of the three inputs resulted in logic "OR" operation (Logic states 1-15), with PSCs failing to cross the threshold of activation (5.5 μA). However, with synchronous firing of the driving inputs V_1, V_2 and the modulatory input V_{ds}, the cumulative PSC increased to a level above the threshold, thereby demonstrating logic "AND" operation (Logic states 15-18), mimicking ion migration across the synaptic membrane causing membrane depolarization. PSC modulation with duty cycle of the inputs, presented in logic states (4-5, 7-8 and 10-11) could be used to design frequency modulated coding schemes, while PSC modulation with presynaptic pulse amplitudes and polarity could be useful for amplitude modulated information coding schemes. With additional drain terminal control, neuronal logic with dynamic gain modulation was realized here with the vesicular release probability being defined by V_{ds} and pulse width of the firing inputs. In accordance with the **probabilistic release model**[28], modulation of EPSCs as a function of pulse width of the presynaptic spikes (defined as **Spike-duration-dependent plasticity (SDDP)**[39]) established temporal causality and feedback for dynamically regulating the vesicular release probability. Increase in V_{ds} dynamically tuned the measured sum exhibiting super-linear behaviour as depicted in Supporting-Information Note-5 figure S6. Positive V_{ds} enhanced the neuronal gain while left-shift of the x-axis intercept changes represented additive operation.[40,41]

Ultra-low Energy Consumption. Despite remarkable progress in emulating synaptic characteristics, current artificial synapses still consume energy that is orders of magnitude greater than their biological counterparts (~10 fJ per synaptic event[42]). Hence, reduction of energy consumption is a primary concern. On comparing the configurations, ionotronic-mode operated at significantly lower power (~4.8 pJ/event) than the electronic-mode (~13 nJ/event), when triggered with the same presynaptic spike (pulse width = 10.5 ms) (Figure 1E, Supporting-Information Note-

6 Table T2). Although still considerably higher than the energy consumption of chemical synapses, ion-mediated gating/ ionotronic-mode seems promising in this regard and provide a significant step toward realizing ultra-low power artificially intelligent electronics. Other recently developed architectures involving stacked hexagonal boron nitride (hBN) - molybdenum disulfide (MoS_2) could allow access to even lower power operation in future.[43] Using a future scaled version of these MoS_2 neuristors (active area = 1 μm^2), the energy consumption per write will account to only 26.67 fJ, better than state-of-the-art memristors[44] and simulated spintronic domain-wall magnets for spiking neural networks.[45]

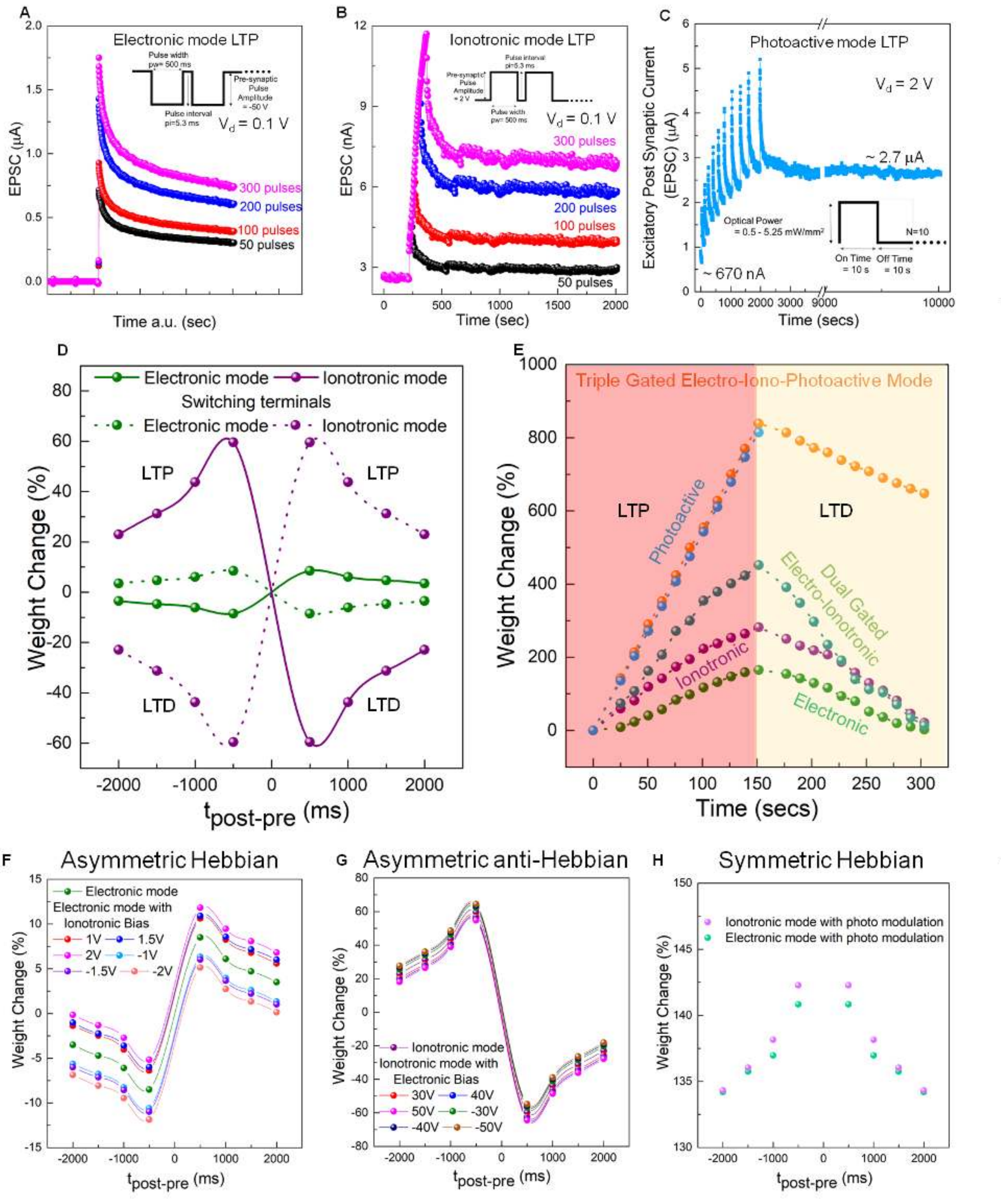

Figure 2. Interplay between Hebbian and Homeostatic Synaptic Plasticity in MoS_2 neuristors. Increment in long-term potentiation (LTP) strength as a function of persistent training in (**A**) electronic-mode (magnified view). Refer to Figure S7-A for non-magnified view. (**B**) ionotronic-mode (**C**) photoactive-mode (variation with increment in light intensity 0.5-5.25 mW/mm^2). (**D**) Spike-timing-dependent plasticity (STDP) and "reverse" STDP (rSTDP) achieved with the electronic and ionotronic-modes respectively. Differences in trapping probabilities modulated the PSCs and relative timing between the output and input spikes modified the strength of synaptic weights through facilitation and depression. Reversal of pre- and post-synaptic terminals resulted in reversal of the STDP protocols, as indicated by the dotted lines. (**E**) Controlled facilitation and depression achieved in our devices with the multi-gated architecture. STDP modulation and homeostatic regulation in (**F**) electronic (Asymmetric Hebbian) and (**G**) ionotronic-mode (Asymmetric anti-Hebbian) of operation. (**H**) Symmetric Hebbian STDP protocol observed in the photoactive-mode of operation.

Leveraging on the comprehensive emulation of short-term synaptic signatures, various gating strategies were designed to program the synaptic weights to achieve non-volatility and long-term plasticity, essential for neuromorphic computing algorithms. While the hybrid ionic-electronic approaches utilized trapping probabilities at the semiconductor-dielectric interface to achieve hysteresis; a novel optical gating approach (photoactive-mode) utilizing defect-assisted slow recombination mechanisms was harnessed next to create long-term changes in the synaptic weight. These approaches were then conclusively combined to tune the synaptic weight with higher modulability and homeostatic stability.

Electrical programming of synaptic weights: Persistent activity-dependent changes in synaptic transmission, such as **long-term potentiation (LTP)** and **long-term depression (LTD)**, are thought to play a critical role in learning and subsequent memory formation. Understanding LTP and LTD reflects how long-lasting memory-associated changes are likely to occur in the central nervous system (CNS) and yield valid insights into the underlying cellular mechanism of learning and memory. In glutamatergic systems, LTP is caused due to high frequency activation of Mg^{2+}sensitive N-methyl-D-aspartate (NMDA) receptors and phosphorylation of α-amino-3-hydroxy-5-methyl-4-isoxazolepropionic acid (AMPA) receptors, resulting in large ion influx (Na^+, K^+, and Ca^{2+}) into the synaptic membranes, creating a larger post-synaptic dendritic spine with an enhanced synaptic strength.[46] In opposition to potentiation, depression decreases the efficacy of a synapse via low frequency activation of phosphatases causing internalization of AMPAr's through dephosphorylation. In this study, LTP and LTD was induced via repeated pre-synaptic training pulses at the gate terminal. Long-term measurements were conducted on fresh samples to avoid effects of history affecting the experiment. While persistent pulsing at -50V activated LTP in the electronic-mode, +2V activated LTP in the ionotronic-mode. A linear increase in weights was observed with increased number of training pulses. Application of 100 facilitating pulses resulted in a weight change of 117 % in the electronic-mode, while a larger increment of 223 % was observed in the ionotronic-mode (figure 2A-B, E). Application of reverse potential resulted in depression or decrease in conductance, the degree of which was again dependent on the total duration of pulsing/biasing and amplitude of the reverse potential. Electronic-mode depicted a higher depression rate with a weight change of 69 % when compared to 54% in the ionotronic-mode. Similar to short-term plasticity, persistent voltage pulses trapped large number of charge carriers at the semiconductor-dielectric interface resulting in the positive (LTP)/negative (LTD) shift of the conductivity depending on the configuration.[24,25,47] Application of opposite-polarity pulses resulted in removal of the trapped electrons leading to a reversal in the observed phenomena. Scanning rates were kept constant in all these measurements to avoid interference of any scanning-rate dependent hysteresis. Such time-dependent channel hysteretic behaviour due to charge-trapping dynamics has been previously observed in 2D TMDC based TFTs via current transient measurements.[47,48] Normalizing to the same writing time, the ionotronic-mode depicted larger retention characteristics indicating slower carrier relaxation dynamics in this mode of operation.

Optical programming of synaptic weights: The highly modulatable photo-generated carrier concentration in atomically-thin 2D chalcogenide channels[49,50] (here MoS_2) unlocks the possibility of addressing synaptic weights with photon pulses, capitalising on high-bandwidth optical communication protocols. Here, a very strong LTP was induced in our devices via a novel optical gating approach (photoactive-mode), with light pulses (λ = 445 nm) serving as the presynaptic inputs. Upon illumination, the conductance increased rapidly initially and then gradually reached ~ 1 order of magnitude above the dark current. On termination of optical illumination, the conductance exhibited a rapid drop, but remained in a high conductance state as depicted in figure 2C, Supporting-Information Note-7 figure S7-B, C. The rapid transitions were attributed to band-to-band transitions, while the long-lasting high conductance change called Persistent photoconductivity (PPC)[51] was attributed to defect or trap centred slow recombination in accordance with the random local potential fluctuation (RLPF) model.[52] Slower decay marked by increased decay times with increasing photon dosage also agreed well with the RLPF model, with more carriers occupying the sites of the local potential minima resulting in a slower recombination. Here, PPC was harnessed to create permanent changes in post-synaptic conductance as shown in figure 2C. Increased photo-dose enhanced device conductance and modulated the decay dynamics. For the highest photo-dose, the device remained in a high-conductivity state (>/= 2.7 μA) for a period > 2 hours, thereby emulating time-dependent stabilization from STP to LTP, called **"consolidation"**[53] in human brain, in congruence with "the multistore model" of human memory by Atkinson and Shiffrin.[8] Utilization of such photon pulses would help unlock novel neural network architectures where light could be used as a global gate to selectively activate a patch of light sensitive neurons interspersed between photo-insensitive neural elements. This design would also enable architectures with far less number of interconnects, mitigating thermal loss and stray signals, hence improving the signal-to-noise ratio. However, eliminating light induced parasitic currents in hybrid-CMOS neural network architectures would remain challenging and would require additional reflective metal shielding structures to block the light from underlying silicon substrate.

Synergistic gating enables "plasticity of plasticity- Metaplasticity" via interplay between Hebbian plasticity and Homeostatic feedback regulation.[54] Temporal correlations between the pre- and post-synaptic spikes created voltage and time dependent weight changes in conductivity, establishing various forms of spike-timing-dependent plasticity (STDP) rules in our systems. A refinement of Hebb's theory, STDP is considered to be the first law of synaptic plasticity and is believed to underlie learning and memory by competitive strengthening and weakening of synapses in neural networks.[55] In glutamatergic connections, strengthening/LTP occurs if the presynaptic action potential precedes the post-synaptic firing ($t_{post-pre} > 0$, where δt is the relative time interval between the pre- and post-synaptic spikes), while presynaptic potentials following post-synaptic spikes ($t_{post-pre} < 0$) causes weakening/LTD. While operation in the electronic-mode helped realize asymmetric Hebbian STDP protocol, ionotronic-mode operation resulted in "reverse" STDP (rSTDP)/asymmetric anti-Hebbian STDP protocol, reflecting co-existence of different coupling mechanisms within the same device (Fig. 2D, Supporting-Information Note-8 figure S8).[56] Co-existence of such multiple forms of synaptic plasticity increases the efficacy of memory storage and processing capacity of artificial neuristors, enabling design of highly efficient novel neural architectures. These distinct types of parallel synaptic plasticity also reflect specific subcellular molecular prerequisites and depend on background brain activity states. For example, Dopamine (DA) and brain-derived neurotrophic factor (BDNF) modulates unique hippocampal STDP at Schaffer collateral (SC)-CA1 synapses.[57] To the best of our knowledge, this is the first demonstration of interplay between multimodal synaptic signatures achieved in a single neural element. Moreover, different trapping probabilities could be coupled to further fine-tune weight changes achieved during facilitation and depression, emulating different molecular pathways and neuromodulators for induction and expression of STDP. This plasticity of plasticity or metaplasticity demonstrated here reflects a dynamic regulation of plasticity via an internal modulation mechanism maintaining the synaptic efficacy within a dynamic range.[54] For example, additive operation of electronic and ionotronic-modes in a dual-gated approach enhanced the degree of facilitation/depression as shown in figure 2E. The weight changes increased with a higher slope of 3.13 when compared to 1.24 and 1.88 for purely electronic and ionotronic-modes respectively. Subtractive mode of operation helped stabilize weight changes in the STDP protocols, analogous to homeostatic negative feedback regulation[58] in biological neural network. Recent findings have revealed homeostatic mechanism to be an on-demand rapid tuning of synaptic strengths in contrast to the popular view of a slow, global phenomenon.[59] Analogous to this, subtractive operation of the several modes was utilized to create a negative feedback mechanism to offset excessive excitation or inhibition by adjusting their synaptic strengths. For example, the device could be configured in a double-gated mode where facilitation caused by electronic-mode could be counteracted by depression of ionotronic-mode and vice-versa (figure 2 F, G). Thus, based on the net coupling of carriers, corresponding weight changes could be programmed with fine precision.

Similarly, operation in photoactive-mode depicted very strong facilitation signatures analogous to runaway dynamics[60] of synaptic weights, but could be regulated by negating homeostatic regulatory electronic and ionotronic-mode of operation via a negative feedback mechanism (figure 2E). Large facilitation in photoconductance (> 800%) was regulated by 22% depression activated by combinatorial operation of electronic and ionotronic-modes within a timescale of 150 seconds. Staying within this time frame, the corresponding STDP protocol exhibited a net facilitation independent of relative time interval between the pre- and post-synaptic voltage spikes, viz. an symmetric Hebbian STDP behaviour (figure 2 E, H). Complete homeostatic compensation was possible at larger time scales (~ 900 seconds). Thus, the positive feedback process of Hebbian plasticity with associative synaptic changes could be regulated by a homeostatic negative feedback process, constraining activity levels and maintaining stability all within a single neural element. With combination of a low intensity photo-dose and high counteracting electrical erasing voltages, it becomes possible to tune this behaviour even further. To the best of our knowledge, this is the first demonstration of interplay between Hebbian and Homeostatic plasticity in a single artificial neural element. Compared to previous works on metaplasticity in memristors that used only pre-synaptic activity-based priming[61,62], a new terminal that may be controlled by pre-synaptic rate or other signals such as similar to neuromodulation by dopaminergic, noradrenergic, muscarinic, and nicotinic receptors[63,64] is realized here. This control gate may also be used to induce homeostasis, enabling neural network operation within its normal dynamic range.[65,66] Hence, this multi-gated optoelectronic approach enables novel artificial neural architectures with multiple operational modes and theoretically infinite plasticity. However, it should be noted that in practical implementations of the mulit-gated approach with metaplasticity, the synapse needs to be disconnected from the neuron on a post-synaptic spike, as is commonly done in other non-volatile memory (NVM) based synaptic plasticity[5,56,67,68] to prevent large surges in EPSCs due to any individual gating inputs from affecting the network dynamics.

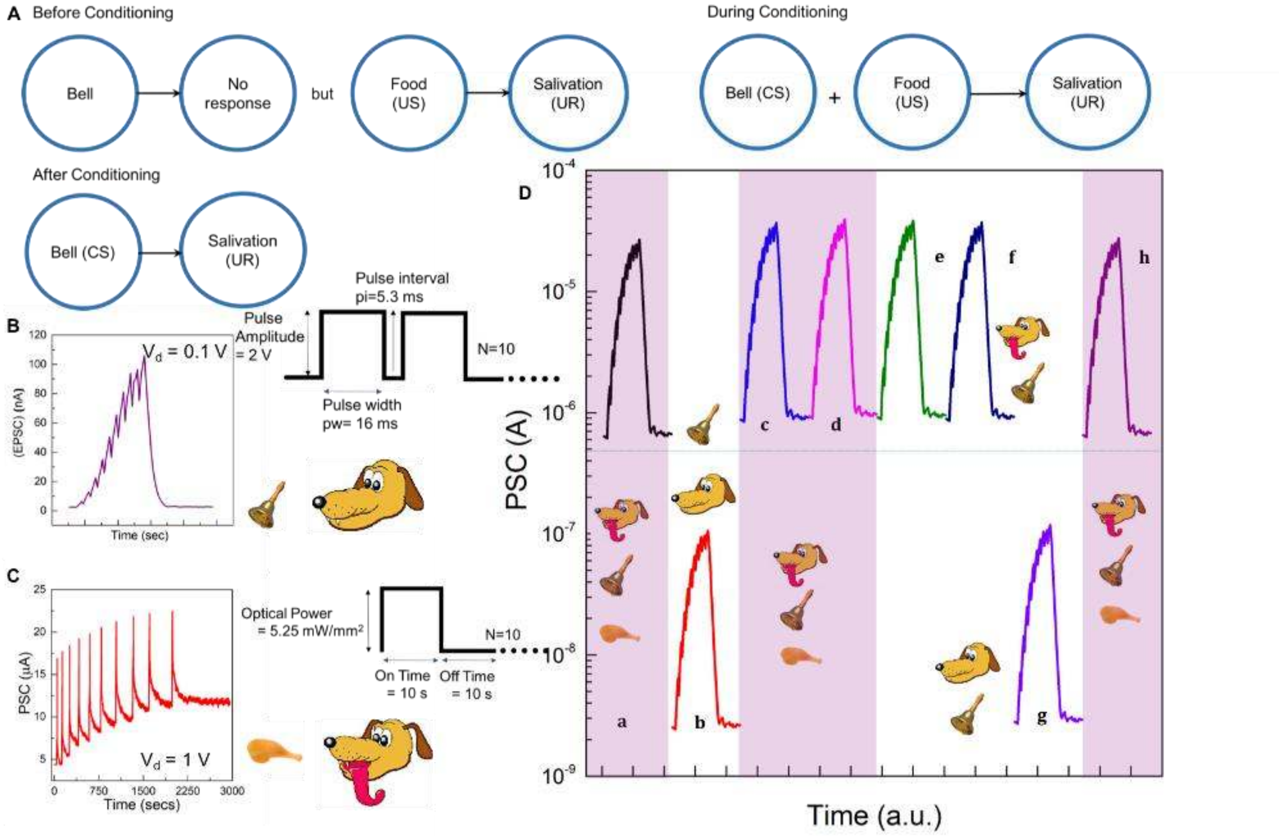

Figure 3. Classical conditioning Pavlov's dog experiment. (**A**) Schematic representing outline of Pavlov's dog experiment. (**B**) Voltage pulses/ conditioned stimulus (CS), (**C**) Optical pulses/unconditioned stimulus (US) and their responses. (**D**) Classical conditioning demonstrated by Pavlov's dog experiment. Initially, light pulses (unconditioned stimulus) led to an efficient unconditioned response (salivation) (state a). However, voltage pulses to the back gate (conditioned stimulus) did not lead to an efficient conditioned response before training (current < 500 nA, no salivation). Initial training sequences with conditioned and unconditioned stimuli did not result in effective association as depicted by state b. Repeated training led to strong association, after which conditioned stimulus alone could trigger salivation (states c-f, current > 500 nA). However, the PSCs decreased below the salivation threshold when triggered by conditioned stimulus alone without accompanying unconditioned stimulus for ~ 2 hours, indicating extinction of associative memory (state g). Finally, the association was recovered back faster with simultaneous conditioned and unconditioned stimuli (state h).

Associative Learning. Finally, the famous **classical conditioning Pavlov's dog experiments**[69,70] (Figure 3, Supporting-Information Note-9 figure S9) were conducted to emulate associative learning in the human brain. In comparison to Pavolovian memristors[69] with temporal dependence of activation signals, this study implements classical conditioning in a thin-film transistor configuration with intimate coupling between optical and electrical pulses, unlocking novel neural network architectures with light as a global gate. Here, light pulses emulated food / unconditioned stimulus (US) activating salivation / unconditioned response (UR) from the post-synaptic terminal, while voltage pulses applied at the back gate emulated bell / conditioned stimulus (CS) for the dog activating a conditioned response (CR). Pavlov's dog started to salivate (unconditioned response) on noticing food (stage a, stimulus of 10 light pulses, λ = 445 nm), marked by a corresponding high-level current output above 500 nA (salivation response threshold). However, at the beginning, the bell ring (stimulus of 10 voltage pulses) alone did not lead to any salivation (current < 500 nA, data not shown). During the initial training routines (10 cycles) with simultaneous feeding and ringing the bell, the post-synaptic currents (PSCs) increased above the salivation response threshold. But conditioned stimulus alone still didn't produce salivation, indicating inefficient response in the dog (stage b). However, on repeated training with simultaneous feeding and ringing the bell (40 cycles), the dog learned to associate the ring (conditioned stimulus) with food (unconditioned stimulus), marked by post-synaptic currents higher than the salivation response threshold (stage c, d). Conditioned response after the 40 training cycles remained so strong that subsequent conditioned stimulus alone clearly produced a high current output higher than the salivation threshold for ~ 2 hours, indicating an efficient association (learning) between the food / unconditioned stimulus and the bell / conditioned stimulus (stage e, f). As a result, Pavlov's dog now salivated when it heard the ringing of the bell alone. Important classical conditioning signatures of **extinction** and **recovery**[71] were also realized in our system. A series of voltage pulses (conditioned stimuli) applied to the "well-trained" dog without accompanying unconditioned stimuli, resulted in decrease of PSC (mimicking depression) below the salivation threshold after ~ 2 hours. This extinction process (stage g) correlated with the elimination of old information in the human brain. This conditioned reflex was again rebuilt or recovered on additional "retraining" (stage h). It was observed that the number of retraining cycles (15) required to re-accomplish the same level of association was less than the initial number of training cycles (20). This in-turn reflected a semi-permanent conductance change due to excessive electron accumulation on repeated learning.

Conclusion. In summary, comprehensive synaptic behaviours were demonstrated for the first time in 2D MoS_2 three-terminal devices with a synergistic multi-gate architecture exhibiting three modes of operation, namely- electronic, ionotronic and photoactive. The memory behaviour was linked to the origin of hysteresis and was attributed to electron trapping-detrapping at the semiconducting channel, migration-relaxation of ions in the IL gate dielectric and slow trap assisted recombination depending on the configuration. Pre-synaptic voltage stimuli first activated STP/STD in our artificial synapse and persistent voltage/optical stimuli consolidated the resistance state to achieve LTP/LTD. Synaptic plasticity was tuned by modulating temporal correlations between presynaptic and post-synaptic action potentials and the three modes were combined to modulate Hebbian STDP plasticity with metaplasticity and homeostatic regulation. Vital characteristics of neurotransmitter release and dynamic logic was realized using frequency, amplitude and synchronicity dependent pulsing algorithms. Finally, classical conditioning was emulated using simultaneous paired stimulation of unconditioned optical and conditioned voltage pulses, resulting in associative learning. Furthermore, the inculcated conditioned response could be extinguished, and recovered under continuous conditioned stimulation and retraining. Compared to previously reported artificial electrical synapses, such optoelectronic synapses pave way for intelligent optical computing systems with ultrafast propagation speed without interconnect issues, and selective activation of neurons and synapses similar to optogenetics. The metaplasticity effect potentially alleviates a lot of network level issues pertaining to statistical variations between synaptic and neuronal elements. However, some of the challenges which have to be overcome for large-scale usage of this technology include development of reliable integration with underlying CMOS electronics, ionically gating large array of transistors and managing the differences in voltage amplitudes between the difference modes of operation.

Experimental Section. A scotch-tape method was used to exfoliate MoS_2 flakes from bulk crystal and was transferred onto a degenerately doped Si substrate with 285 nm SiO_2. The thin flakes were identified by optical contrast conducted with Olympus BX51 microscope. Raman and photoluminescence characterizations were performed using Witec confocal Raman system under 532 nm laser excitation. The electrodes were patterned via photolithography, followed by thermal evaporation of Cr/Au (5/50 nm) and subsequent lift-off process. Electrical measurements were carried out using Keithley 4200-SCS semiconductor characterization system via custom defined pulsing programs with a coupled light source (Thorlabs Solis-445C) and a DC2200 driver in an external Transistor–transistor logic (TTL) modulation configuration.

Supporting Information

Supporting Information is available from the Wiley Online Library or from the author.

Acknowledgements.

R.A.J. and F.L. contributed equally to this work. The authors would like to acknowledge the funding from MOE Tier 1 grant RG 166/16, MOE Tier 2 grants MOE2016-T2-1-100, MOE2015-T2-2-007 and from National Research Foundation under NRF RF Award No. NRF-RF2013-08.

References.

[1] M. M. Waldrop, Nature 2012, 482, 456.
[2] S. Herculano-Houzel, Front. Hum. Neurosci. 2009, 3.
[3] L. F. Abbott, S. B. Nelson, Nat. Neurosci. 2000, 3, 1178.
[4] W. Gerstner, W. M. Kistler, R. Naud, L. Paninski, Neuronal Dynamics: From Single Neurons to Networks and Models of Cognition, Cambridge University Press, Cambridge, 2014.
[5] R. Gopalakrishnan, A. Basu, IEEE Trans. neural networks Learn. Syst. 2017, 28, 778.
[6] G. Indiveri, S.-C. Liu, Proc. IEEE 2015, 103, 1379.
[7] Z. Wang, S. Joshi, S. E. Savel'ev, H. Jiang, R. Midya, P. Lin, M. Hu, N. Ge, J. P. Strachan, Z. Li, Nat. Mater. 2017, 16, 101.
[8] T. Ohno, T. Hasegawa, T. Tsuruoka, K. Terabe, J. K. Gimzewski, M. Aono, Nat. Mater. 2011, 10, 591.
[9] M. Prezioso, F. Merrikh-Bayat, B. D. Hoskins, G. C. Adam, K. K. Likharev, D. B. Strukov, Nature 2015, 521, 61.
[10] G. Indiveri, B. Linares-Barranco, T. J. Hamilton, A. Van Schaik, R. Etienne-Cummings, T. Delbruck, S.-C. Liu, P. Dudek, P. Häfliger, S. Renaud, Front. Neurosci. 2011, 5, 73.
[11] Y. van de Burgt, E. Lubberman, E. J. Fuller, S. T. Keene, G. C. Faria, S. Agarwal, M. J. Marinella, A. A. Talin, A. Salleo, Nat. Mater. 2017, 16, 414.
[12] Y. Zang, H. Shen, D. Huang, C. Di, D. Zhu, Adv. Mater. 2017, 29.

[13] P. Gkoupidenis, D. A. Koutsouras, G. G. Malliaras, Nat. Commun. 2017, 8.
[14] J. Shi, S. D. Ha, Y. Zhou, F. Schoofs, S. Ramanathan, Nat. Commun. 2013, 4.
[15] L. Q. Zhu, C. J. Wan, L. Q. Guo, Y. Shi, Q. Wan, Nat. Commun. 2014, 5.
[16] R. A. John, J. Ko, M. R. Kulkarni, N. Tiwari, N. A. Chien, N. Geok, W. L. Leong, N. Mathews, Small 2017, 13.
[17] X. Hong, J. Kim, S.-F. Shi, Y. Zhang, C. Jin, Y. Sun, S. Tongay, J. Wu, Y. Zhang, F. Wang, Nat. Nanotechnol. 2014, 9, 682.
[18] B. Radisavljevic, A. Radenovic, J. Brivio, i V Giacometti, A. Kis, Nat. Nanotechnol. 2011, 6, 147.
[19] K. Kang, S. Xie, L. Huang, Y. Han, P. Y. Huang, K. F. Mak, C.-J. Kim, D. Muller, J. Park, Nature 2015, 520, 656.
[20] S. Mouri, Y. Miyauchi, K. Matsuda, Nano Lett. 2013, 13, 5944.
[21] H. J. Conley, B. Wang, J. I. Ziegler, R. F. Haglund Jr, S. T. Pantelides, K. I. Bolotin, Nano Lett. 2013, 13, 3626.
[22] N. Vitureira, Y. Goda, J Cell Biol 2013, 203, 175.
[23] A. M. Shen, C.-L. Chen, K. Kim, B. Cho, A. Tudor, Y. Chen, ACS Nano 2013, 7, 6117.
[24] A. J. Arnold, A. Razavieh, J. R. Nasr, D. S. Schulman, C. M. Eichfeld, S. Das, ACS Nano 2017, 11, 3110.
[25] J. Jiang, J. Guo, X. Wan, Y. Yang, H. Xie, D. Niu, J. Yang, J. He, Y. Gao, Q. Wan, Small 2017.
[26] S. Nakanishi, Science (80-.). 1992, 258, 597.
[27] J. Del Castillo, B. Katz, J. Physiol. 1954, 124, 560.
[28] T. Branco, K. Staras, Nat. Rev. Neurosci. 2009, 10, 373.
[29] R. S. Zucker, Annu. Rev. Neurosci. 1989, 12, 13.
[30] J. C. López, Nat. Rev. Neurosci. 2001, 2, 307.
[31] G. Perea, A. Araque, Science (80-.). 2007, 317, 1083.
[32] J. T. Coyle, P. Puttfarcken, Science (80-.). 1993, 262, 689.
[33] M. A. Castro-Alamancos, B. W. Connors, Proc. Natl. Acad. Sci. 1996, 93, 1335.
[34] G. Buzsáki, A. Draguhn, Science (80-.). 2004, 304, 1926.
[35] L. F. Abbott, W. G. Regehr, Nature 2004, 431, 796.
[36] J. M. J. Murre, J. Dros, PLoS One 2015, 10, e0120644.
[37] A. N. Burkitt, Biol. Cybern. 2006, 95, 97.
[38] A. N. Burkitt, Biol. Cybern. 2006, 95, 1.
[39] W. Xu, H. Cho, Y. H. Kim, Y. T. Kim, C. Wolf, C. G. Park, T. W. Lee, Adv. Mater. 2016, 28, 5916.
[40] F. S. Chance, L. F. Abbott, A. D. Reyes, Neuron 2002, 35, 773.
[41] E. Salinas, P. Thier, Neuron 2000, 27, 15.
[42] W. Xu, S.-Y. Min, H. Hwang, T.-W. Lee, Sci. Adv. 2016, 2, e1501326.
[43] G.-H. Lee, Y.-J. Yu, X. Cui, N. Petrone, C.-H. Lee, M. S. Choi, D.-Y. Lee, C. Lee, W. J. Yoo, K. Watanabe, ACS Nano 2013, 7, 7931.
[44] I. Gupta, A. Serb, A. Khiat, R. Zeitler, S. Vassanelli, T. Prodromakis, Nat. Commun. 2016, 7.
[45] G. Narasimman, S. Roy, X. Fong, K. Roy, C.-H. Chang, A. Basu, in Circuits Syst. (ISCAS), 2016 IEEE Int. Symp., IEEE, 2016, pp. 914–917.
[46] G. L. Collingridge, T. V. P. Bliss, Trends Neurosci. 1987, 10, 288.
[47] H. Tian, Q. Guo, Y. Xie, H. Zhao, C. Li, J. J. Cha, F. Xia, H. Wang, Adv. Mater. 2016, 28, 4991.
[48] I. Amit, T. J. Octon, N. J. Townsend, F. Reale, C. D. Wright, C. Mattevi, M. F. Craciun, S. Russo, Adv. Mater. 2017, 29.
[49] O. Lopez-Sanchez, D. Lembke, M. Kayci, A. Radenovic, A. Kis, Nat. Nanotechnol. 2013, 8, 497.
[50] D. Kufer, G. Konstantatos, Nano Lett. 2015, 15, 7307.
[51] K. Roy, M. Padmanabhan, S. Goswami, T. P. Sai, G. Ramalingam, S. Raghavan, A. Ghosh, Nat. Nanotechnol. 2013, 8, 826.
[52] Y.-C. Wu, C.-H. Liu, S.-Y. Chen, F.-Y. Shih, P.-H. Ho, C.-W. Chen, C.-T. Liang, W.-H. Wang, Sci. Rep. 2015, 5.
[53] T. V Bliss, G. L. Collingridge, Nature 1993, 361, 31.

[54] W. C. Abraham, M. F. Bear, Trends Neurosci. 1996, 19, 126.
[55] S. Song, K. D. Miller, L. F. Abbott, Nat. Neurosci. 2000, 3, 919.
[56] S. Brink, S. Nease, P. Hasler, S. Ramakrishnan, R. Wunderlich, A. Basu, B. Degnan, IEEE Trans. Biomed. Circuits Syst. 2013, 7, 71.
[57] E. Edelmann, E. Cepeda-Prado, V. Leßmann, Front. Synaptic Neurosci. 2017, 9, 7.
[58] G. G. Turrigiano, S. B. Nelson, Nat. Rev. Neurosci. 2004, 5, 97.
[59] K. Pozo, Y. Goda, Neuron 2010, 66, 337.
[60] F. Zenke, E. J. Agnes, W. Gerstner, Nat. Commun. 2015, 6, 6922.
[61] X. Zhu, C. Du, Y. Jeong, W. D. Lu, Nanoscale 2017, 9, 45.
[62] Z. Tan, R. Yang, K. Terabe, X. Yin, X. Zhang, X. Guo, Adv. Mater. 2016, 28, 377.
[63] N. Frémaux, W. Gerstner, Front. Neural Circuits 2016, 9, 85.
[64] V. Pawlak, J. R. Wickens, A. Kirkwood, J. N. D. Kerr, Front. Synaptic Neurosci. 2010, 2, 146.
[65] A. J. Watt, N. S. Desai, Front. Synaptic Neurosci. 2010, 2, 5.
[66] C. Clopath, L. Büsing, E. Vasilaki, W. Gerstner, Nat. Neurosci. 2010, 13, 344.
[67] T. Serrano-Gotarredona, T. Masquelier, T. Prodromakis, G. Indiveri, B. Linares-Barranco, Front. Neurosci. 2013, 7, 2.
[68] S. Ramakrishnan, P. E. Hasler, C. Gordon, IEEE Trans. Biomed. Circuits Syst. 2011, 5, 244.
[69] I. P. Pavlov, G. V. Anrep, Conditioned Reflexes, Courier Corporation, 2003.
[70] Z.-H. Tan, X.-B. Yin, R. Yang, S.-B. Mi, C.-L. Jia, X. Guo, Sci. Rep. 2017, 7, 713.
[71] C. Wu, T. W. Kim, T. Guo, F. Li, D. U. Lee, J. J. Yang, Adv. Mater. 2017, 29.

Table of Contents (ToC)

Synergistic Gating of Electro-Iono-Photoactive 2D Chalcogenide Neuristors: co-existence of Hebbian and Homeostatic Synaptic Metaplasticity

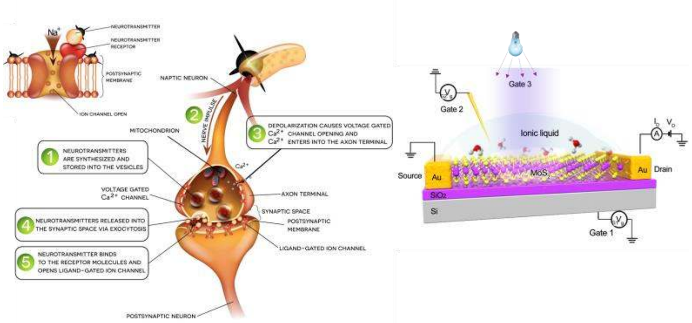
Na^+
NEUROTRANSMITTER
NEUROTRANSMITTER RECEPTOR
POSTSYNAPTIC MEMBRANE
ION CHANNEL OPEN
NAPTIC NEURON
NERVE IMPULSE
2
MITOCHONDRION
3 DEPOLARIZATION CAUSES VOLTAGE GATED Ca^{2+} CHANNEL OPENING AND Ca^{2+} ENTERS INTO THE AXON TERMINAL
1 NEUROTRANSMITTERS ARE SYNTHESIZED AND STORED INTO THE VESICLES
Ca^{2+}
VOLTAGE GATED Ca^{2+} CHANNEL
AXON TERMINAL
SYNAPTIC SPACE
POSTSYNAPTIC MEMBRANE
4 NEUROTRANSMITTERS RELEASED INTO THE SYNAPTIC SPACE VIA EXOCYTOSIS
5 NEUROTRANSMITTER BINDS TO THE RECEPTOR MOLECULES AND OPENS LIGAND-GATED ION CHANNEL
LIGAND-GATED ION CHANNEL
POSTSYNAPTIC NEURON
Gate 3
V_{g2}
Gate 2
Ionic liquid
I_D V_D
A
Source
Au
MoS_2
Au
Drain
SiO_2
Si
V_{g1}
Gate 1

Emulation of brain-like signal processing lays the foundation for building artificial neural networks. Exploiting a novel multi-gated architecture incorporating electrical and optical biases, MoS_2 neuristors are realized here to mimic biological intracellular ion flux with dynamic control of Hebbian metaplasticity and Homeostatic regulation. Encompassing higher functionalities into single artificial neurons will mitigate high circuit density requirements necessary to match the computational complexity of the human brain.

Rohit Abraham John[1†], *Fucai Liu*[1†], *Nguyen Anh Chien*[1], *Mohit R. Kulkarni*[1], *Chao Zhu*[1], *Qundong Fu*[1], *Arindam Basu*[2], *Zheng Liu*[1], *Nripan Mathews*[1,3]*

[†]These authors contributed equally in this work

* Corresponding author

Prof. Nripan Mathews (Email: Nripan@ntu.edu.sg)

Synergistic Gating of Electro-Iono-Photoactive 2D Chalcogenide Neuristors: co-existence of Hebbian and Homeostatic Synaptic Metaplasticity

Rohit Abraham John[1†], *Fucai Liu*[1†], *Nguyen Anh Chien*[1], *Mohit R. Kulkarni*[1], *Chao Zhu*[1], *Qundong Fu*[1], *Arindam Basu*[2], *Zheng Liu*[1], *Nripan Mathews*[1,3]*

[1] School of Materials Science and Engineering, Nanyang Technological University, 50 Nanyang Avenue, Singapore 639798

[2] School of Electrical and Electronic Engineering, Nanyang Technological University, 50 Nanyang Avenue, Singapore 639798

[3] Energy Research Institute @ NTU (ERI@N), Nanyang Technological University, Singapore 637553

[†]These authors contributed equally in this work

* Corresponding author

Prof. Nripan Mathews (Email: Nripan@ntu.edu.sg)

Keywords: 2D chalcogenides, Neuromorphic Computing, Hebbian Synaptic Plasticity, Homeostatic regulation, Associative learning

Note 1: Physical Characterization of MoS_2

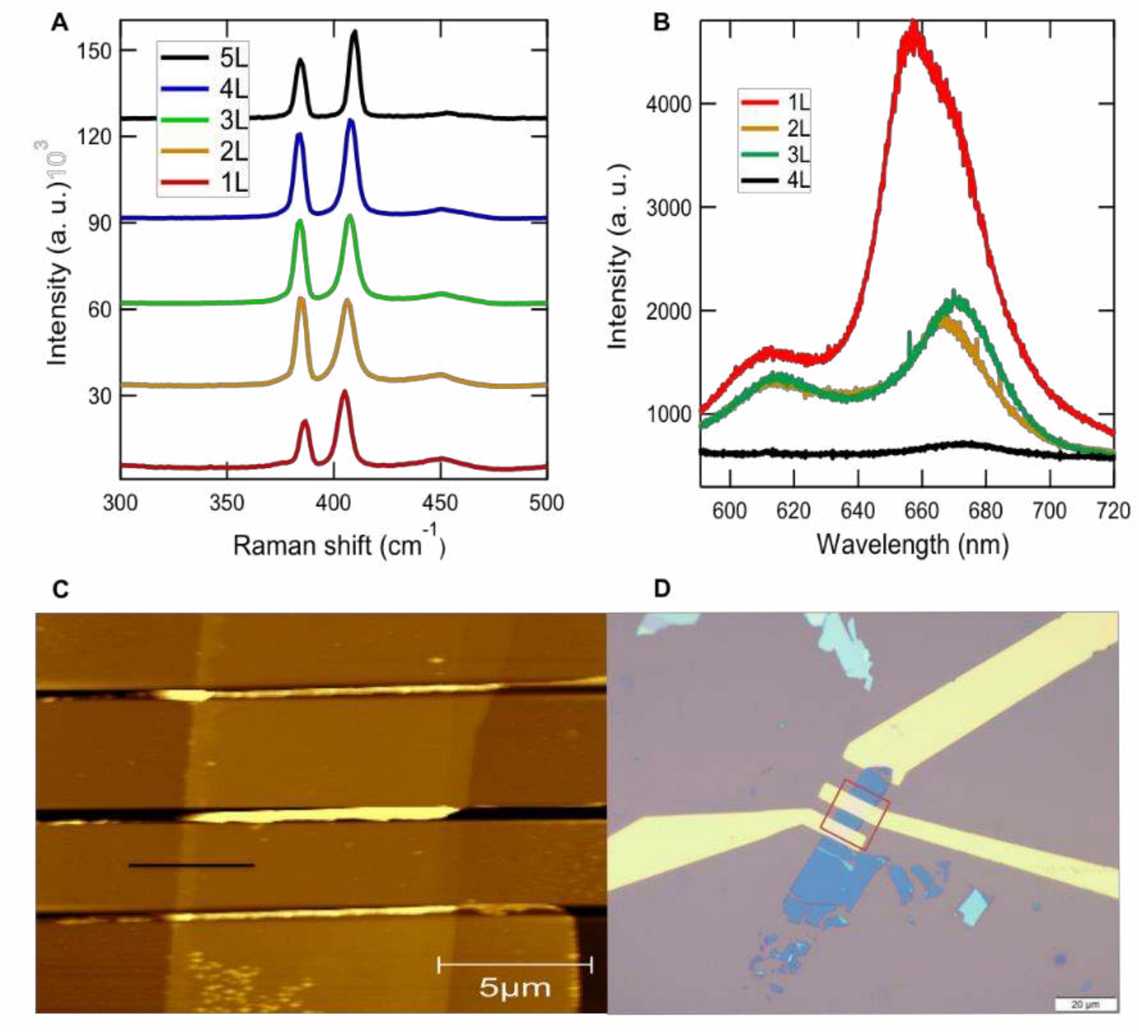

Figure S1. (**A**) Raman-spectra of multilayer MoS_2 flake depicting the in-plane E^1_{2g} mode and the out-of-plane A_{1g} mode. (**B**) PL spectra indicating transition from direct to indirect bandgap with increasing number of MoS_2 layers. (**C**) AFM image at the MoS_2 flake edge. (**D**) Optical image of the MoS_2 flake.

Raman and PL characterizations of MoS_2 were conducted on samples of different thickness. As shown in Fig. S1-A, the Raman spectrum depicted two typical peaks around 386 cm^{-1} (E^1_{2g}) and 405 (E_{1g}) cm^{-1} peaks. A blue shift of A_{1g} and red shift of E^1_{2g} was observed with increasing number of MoS_2 layers. This opposite direction of the frequency shift has been partly attributed to the Columbic interaction and possible stacking-induced change in intra-layer bonding.[1] Due to the quantum confinement effect, MoS_2 crystal showed a crossover from the indirect bandgap in bulk to direct in monolayer form.[2] As shown in Fig. S1-B, the PL intensity of monolayer MoS_2 was much stronger than that of the bi-layer and tri-layer samples, indicating the direct band gap nature of monolayer MoS_2. Fig. S1C-D shows the AFM and optical images of the MoS_2 devices.

Note 2: Mobility extraction and Possible origin of hysteresis

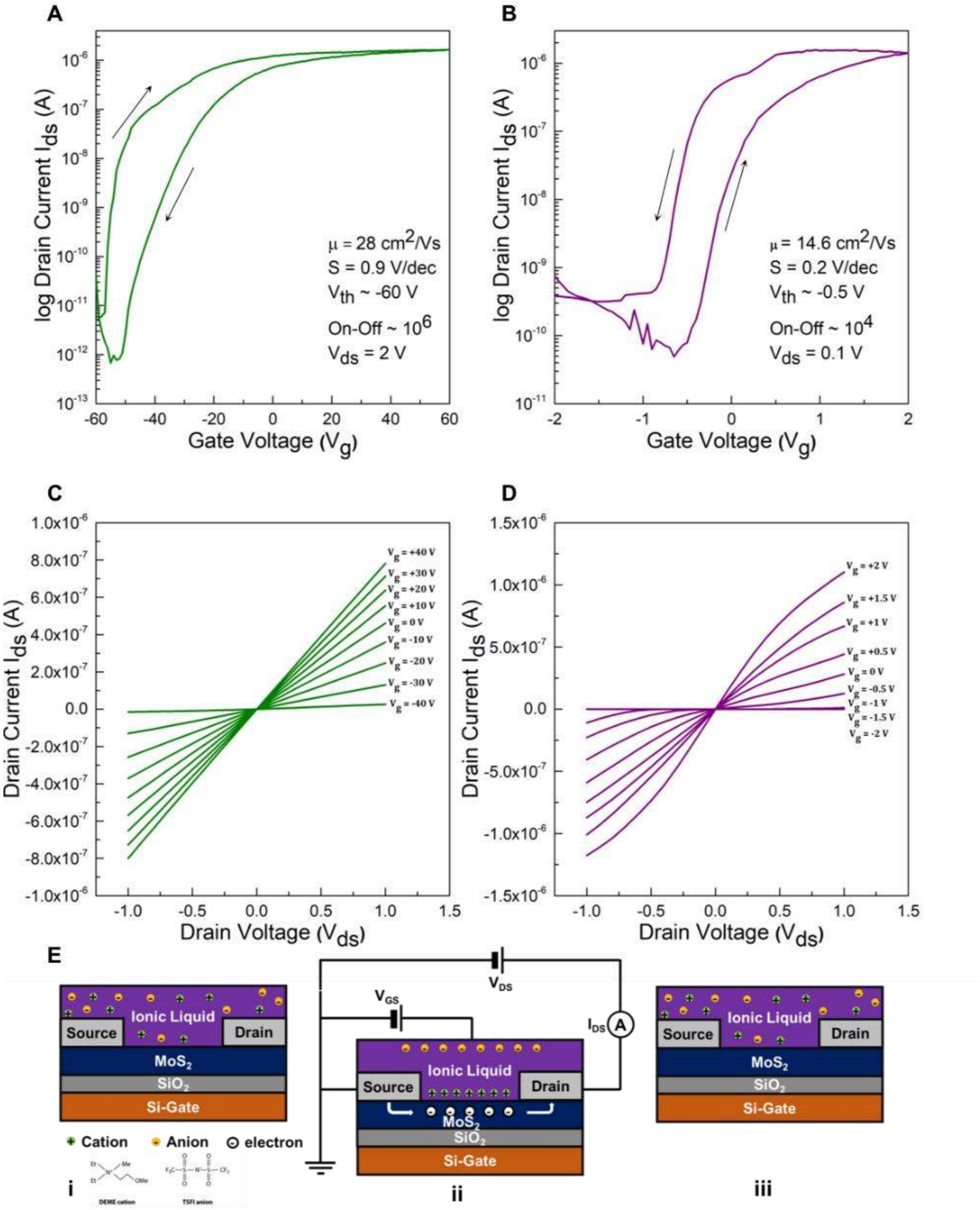

Figure S2. Transfer characteristics of (A) Back-gated MoS_2 – SiO_2 architecture (electronic-mode) (B) Top gated MoS_2 – IL configuration (ionotronic-mode). Output characteristics of devices in (C) electronic-mode and (D) ionotronic-mode. (E) Working principle of ionotronic MoS_2 electric-double-layer (EDL) transistors. (i) initial state of the ions in the ionic liquid dielectric before voltage is applied. (ii) on application of positive gate voltage pulse, cations (DEME) in the ionic liquid-polymer dielectric migrate and accumulate at the dielectric-semiconductor interface inducing a

channel current in the MoS_2 semiconducting layer. (iii) on removal of gate voltage pulse, the DEME cations gradually relax back to their initial positions, reducing channel conductivity and the drain current gradually decreases back to the resting current.

The field-effect mobility was estimated from the linear region in the I_d- V_g curve (V_g from 10 V to 30 V) by using the equation $\mu = \frac{\mathrm{d}I_d}{\mathrm{d}V_g} \times \frac{L}{WC_iV_d}$, where L is the channel length (mention exactly), W is the channel width and C_i is the capacitance between the channel and the back gate per unit area ($C_i = \varepsilon_0\varepsilon_r / d$; ε_0 is the vacuum permittivity, ε_r is the relative permittivity, and d is the thickness of SiO_2 layer), respectively. The channel length and channel width of the device were ~ 9 µm and ~ 20 µm, respectively and thickness of the MoS_2 flake was 9 nm. The mobility was calculated to be around 28 $cm^2V^{-1}s^{-1}$ for the electronic-mode, which is in the same order as the reported value.[3] For ionotronic-mode, the capacitance was taken as 1.55 µF/cm^2 for **DEMETFSI** from a previous study,[4] and the mobility was calculated to be around 14.6 $cm^2V^{-1}s^{-1}$. The small electrochemical window of the ionic liquid limited the operational voltage range to -2 V to +2 V, but the large electrical-double-layer (EDL) capacitance allowed reliable switching in the ionotronic-mode within the small operational voltage window.

From figure S2, devices in electronic-mode clearly depicted a clockwise hysteresis window of 8 V, while ionotronic-mode exhibited an anticlockwise hysteresis window of 0.5 V. In the case of electronic-mode, earlier investigations have indicated three possible origins for the observed clockwise hysteresis. According to the first theory, surface adsorbed moisture and O_2 molecules trapped electrons at positive voltages, thereby depleting the MoS_2 channel and leading to a positive V_{th} shift, while electron detrapping at negative voltages weakened carrier depletion in the channel, leading to a negative shift of V_{th}.[5] The second theory banked on defects at the MoS_2 - SiO_2 interface[6,7], while the third theory suggested intrinsic surface defects on MoS_2 to be responsible for this trapping-detrapping mechanism.[8] In our case, the first and third theory could be ruled out as all measurements were done in high vacuum (10^{-7} mbar), thereby minimizing the probability of surface defects/adsorbates. Hence the hysteresis behaviour observed in the electronic-mode, could be attributed to interfacial defects at the semiconductor-dielectric interface, trapping and detrapping electrons in the forward and reverse voltage scans. In the case of devices in ionotronic-mode, the anticlockwise hysteresis was attributed to mobile cations in the dielectric and its slow relaxation kinetics, which in turn doped and de-doped the channel based on the direction of voltage scan. Forward scan resulted in migration of cations in the IL-polymer dielectric toward the dielectric (IL) – semiconductor (MoS_2) interface, in turn accumulating electrons in the MoS_2 layer to form a conductive channel. This in turn resulted in the requirement of a lower voltage for channel formation in the reverse scan, emanating in anticlockwise hysteresis.

Note 3: Synaptic Transmission Steps

In a biological neural network, electrical impulses collected by dendritic inputs of the presynaptic neuron are processed at the soma, and the subsequent information is transferred to dendrites of post-synaptic neurons via the axon output terminal. Such axo-dendritic neuronal junctions, elemental to information propagation in the central nervous system (CNS) are called synapses. In the inactive state, electrical potential inside a neuron is maintained negative when compared to the extracellular fluid. This potential difference across the neuronal membrane, called resting potential (-70 mV) is maintained by a transport protein called the sodium-potassium pump. On arrival of a stimulus, the neuron transmits action potential impulses causing voltage gated sodium (Na^+) channels in the neuronal membrane to open, thereby reversing the membrane polarity (depolarization) and triggering subsequent action potentials on reaching a threshold (-55 mV). The peak voltage of the action potential then causes the voltage gated sodium channels to close and potassium channels to open, thereby repolarizing and hyperpolarizing the membrane. The neuron then enters a refractory period, where the sodium-potassium pump is reactivated, moving Na^+ and K^+ ions out and in to cell respectively, thereby, returning the neuron to its normal polarized state. During depolarization, voltage-dependent calcium (Ca^{2+}) channels on the presynaptic membrane open up, causing an influx of Ca^{2+} ions. These bind with the membrane of the synaptic vesicles, causing the vesicles to break and releasing neurotransmitters into the synaptic cleft. These neurotransmitters diffuse across the synaptic cleft, interact with binding sites on the postsynaptic receptors and initiate the opening of neurotransmitter-dependent ion channels, thereby depolarizing or hyperpolarizing the postsynaptic membrane resulting in excitatory or inhibitory postsynaptic potentials. This postsynaptic potential reflects the strength of synaptic weight and is defined as synaptic plasticity.[9,10]

Therefore, in such chemical synapses, the release of neurotransmitters mediates transduction of electrical signals into chemical signals, which in turn forms the basis of decision making. Neurotransmitter release is governed by three classical features: (i) excitatory and inhibitory release, (ii) quantal release and (iii) stochastic or probabilistic release. Through weight changes in the postsynaptic currents (PSCs), a combination of these three features determine short and long-term plasticity, thereby controlling various complex emotional, behavioural, learning and psychological functions.[11–13] Therefore, hardware implementation of thin film devices that can emulate selectively permeable ion movement across the synaptic membrane or in other words bio-realistically mimic the neurotransmitter release, could hold the key to developing artificially intelligent machines with learning ability and subjective logic.

Note 4: Emulating excitatory/inhibitory nature of neurotransmitter release

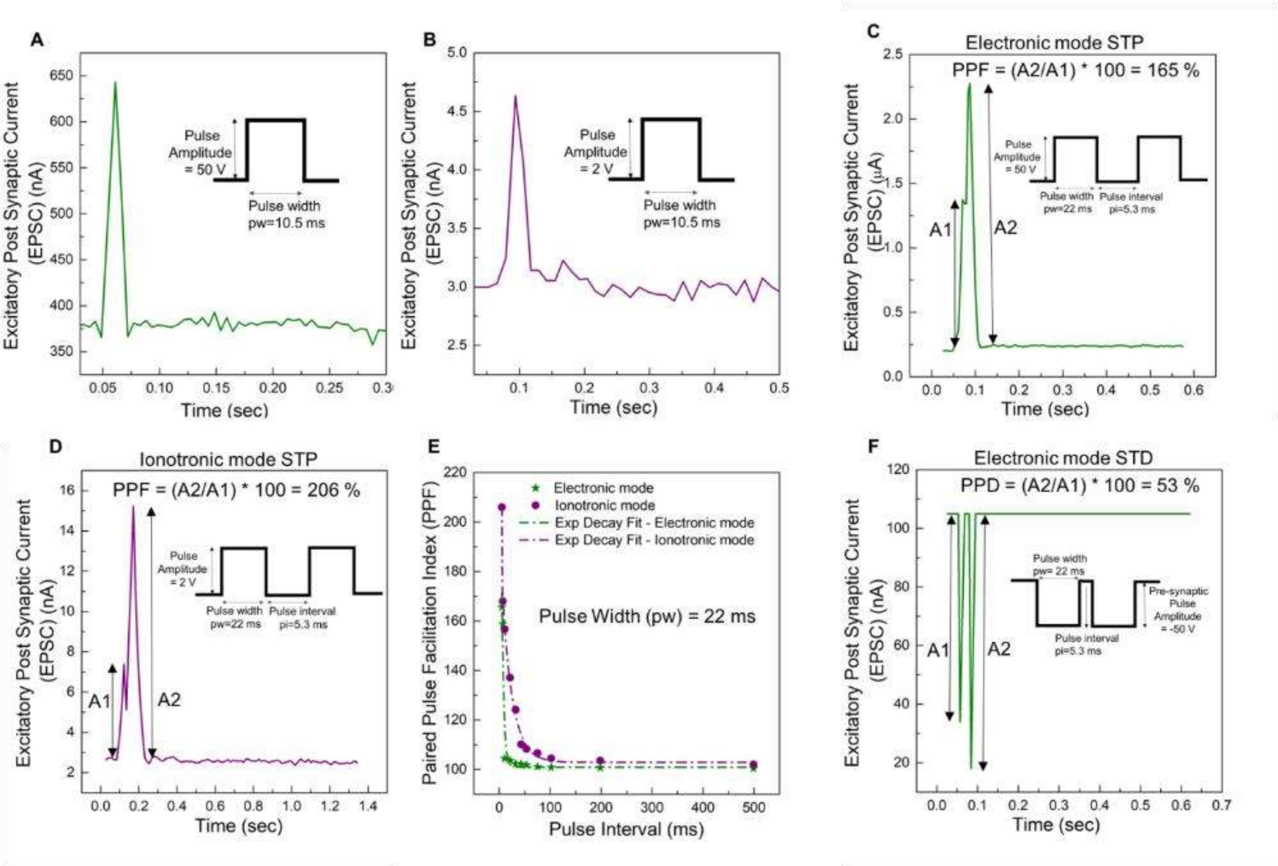

Figure S3. A single presynaptic spike input induces an excitatory postsynaptic current (EPSC) response in (A) electronic-mode, (B) ionotronic-mode. The current abruptly increases on application of the voltage spike and decays back to the resting current on removal of the voltage spike. A pair of presynaptic spikes (pulse width = 22 ms, interval = 5.3 ms) triggered a pair of EPSCs, with amplitude of the 2nd (A2) higher than the 1st (A1). This indicated facilitation due to carrier trapping / ionic retention in (**C**) electronic-mode, (**D**) ionotronic-mode respectively. (**E**) PPF index, defined as the ratio of A2/A1, that is $[PPF = \left(\frac{A2}{A1}\right) * 100\%)]$ is plotted as a function of inter-spike interval to demonstrate the facilitation decay. It quantifies the degree of facilitation and reflects the synaptic vesicular release probability. It also gives an indication of the amount of residual and active Ca^{2+} according to the residual Ca^{2+} hypothesis by Katz and Miledi.[14] In neuroscience, PPF is responsible for cognitive abilities involving temporal processes and determines the degree of associative learning. (**F**) Short-term depression emulated in electronic-mode synapses.

Excitatory post synaptic currents (EPSCs): Post synaptic currents (I_{ds}) were recorded from the drain terminal as a function of the presynaptic potentials (V_g) applied at the gate terminal. While +50 V activated EPSCs to a level of 643 nA from its resting current of ~350 nA for electronic-mode operation; +2 V was used to activate EPSCs to 4.6 nA from its resting current of ~3 nA for the ionotronic-mode for a pulse width of 10.5 ms (Fig S3-A, B). On removal of the presynaptic pulse, current decayed back to its resting level of ~350 nA and ~3 nA for electronic and ionotronic-modes respectively.

Paired-pulse facilitation (PPF) : When a synapse with low initial probability of vesicle release is stimulated in rapid succession, the second post-synaptic response can be larger than the first - a phenomenon called neural facilitation or paired-pulse facilitation (PPF).[15] In a chemical synapse, temporally correlated action potentials cause voltage-gated Ca^{2+} channels to open, resulting in Ca^{2+} influx and higher presynaptic active calcium (Ca^{2+}) concentration. This in turn triggers synaptic vesicles to release large amounts of neurotransmitters into the synaptic cleft. PPF index, which is the ratio of the amplitude of the second response to that of the first, could be used to quantify facilitation of excitatory post-synaptic currents (EPSC) and is an easy measure of synaptic vesicular release probability.[16] PPF is an exclusive presynaptic phenomenon as per the residual Ca^{2+} hypothesis by Katz and Miledi[16], according to which residual Ca^{2+} after the first impulse caused an increase in neurotransmitter release following the second stimulus. The degree of facilitation is determined by the amount of active Ca^{2+}, and is greatest when the Ca^{2+} ions are not allowed to return to the baseline concentration prior to the second stimulus, that is, when the pulse interval is kept shortest. In the opposite scenario, decreased vesicular release probability and inactivation of voltage-gated Ca^{2+} could lead to short-term depression (STD), usually seen in synapses with high probability of initial vesicle release.

In our study, when the pulse interval was kept small (< 30 ms), EPSC triggered by the second presynaptic spike was observed to be much higher than one triggered by the first spike, indicating a strong facilitation (PPF index >> 100%). For electronic-mode, the maximum PPF index observed was ~165%, while ionotronic-mode depicted a much higher facilitation ratio of ~206% for a pulse interval of 5.3 ms. This ratio continued to decrease with increasing pulse interval and finally reached around 100 % for the largest pulse interval of 500 ms. This observed decay of PPF index with pulse interval was fitted with a exponential function[17] in resemblance to a chemical synapse

(Figure S3-C-E, Table-T1). PPF index of type-I synaptic TFTs drastically reduced from 165% to ~100% as the pulse interval increased from 5.3 ms to 10.7 ms respectively. On the other hand, PPF decay was much slower for type-II synaptic TFTs with the PPF index well above 100% for pulse interval up to 100 ms, indicating a larger facilitation window for the same. In resemblance to the coupling of biological neurons, PPF variation with pulse interval fitted well with an exponential decay function as shown below.

$$y = B_1 * \exp\left(-\frac{x}{t_1}\right) + B_2 * \exp\left(-\frac{x}{t_2}\right) + y_0$$

where x is pulse interval time, y_0 is resting facilitation magnitude, B_1 & B_2 are facilitation constants, and t_1 and t_2 are characteristic time constants of the rapid and slow phases. Detailed comparison of the decay time constants is presented in table T1 below.

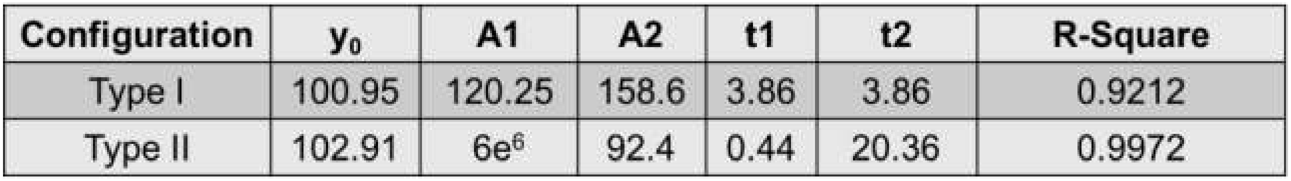

Configuration	y_0	A1	A2	t1	t2	R-Square
Type I	100.95	120.25	158.6	3.86	3.86	0.9212
Type II	102.91	$6e^6$	92.4	0.44	20.36	0.9972

Table T1. Best fit values of PPF decay as a function of pulse interval.

In the electronic-mode of operation, interfacial traps modulated the resistance state and mimicked flux of Ca^{2+} ions/neurotransmitter release by the trapping-detrapping mechanism. For the ionotronic-mode, the neurotransmitter release was mimicked by the ion migration-relaxation kinetics at the semiconductor-dielectric interface. In both scenarios, charge transport pathways emulated the synaptic cleft and the channel conductance defined synaptic weight.

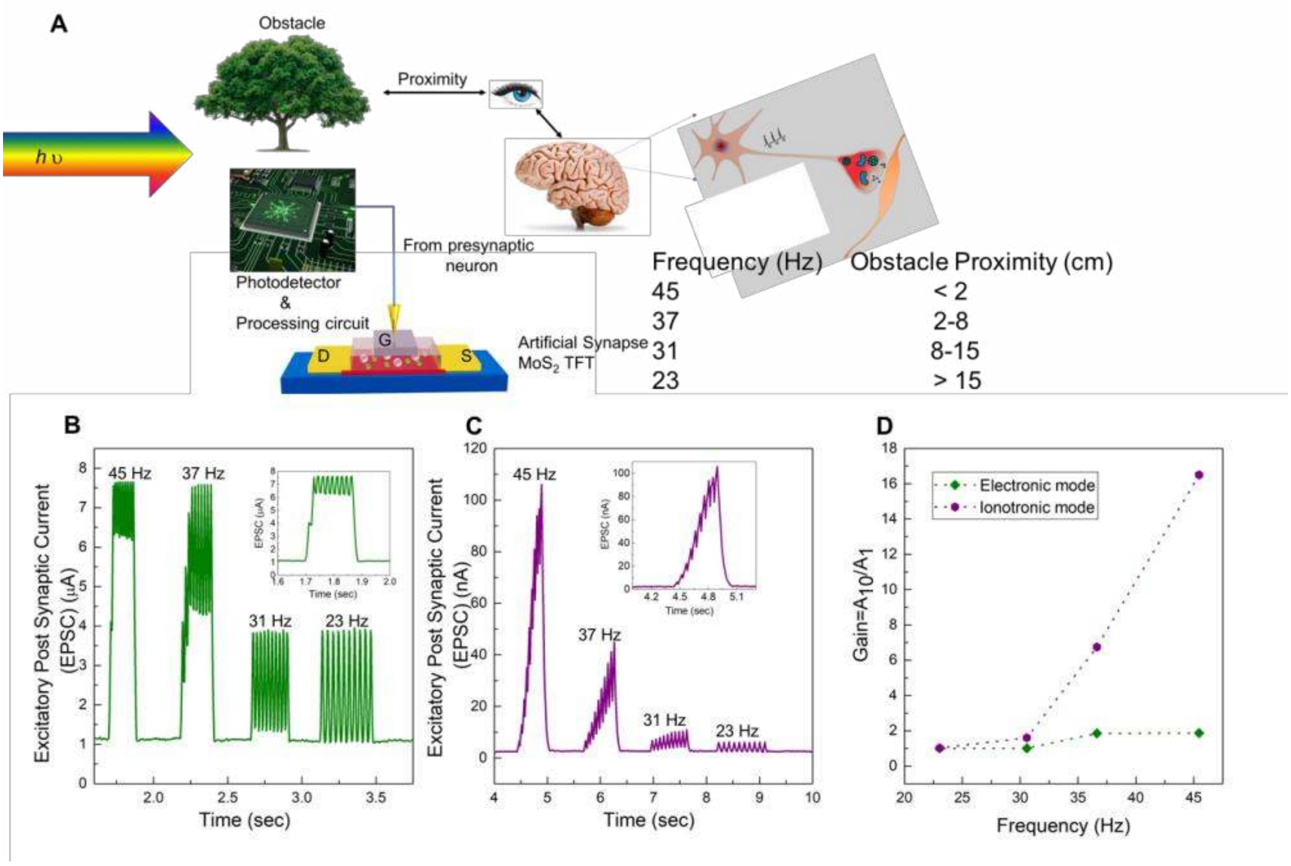

Figure S4. (A) Schematic representation of the neural communication between sensory neurons and brain. The artificial synapse was integrated with a LDR via a microprocessing circuit for obstacle detection. EPSCs in response to presynaptic trains of different frequencies corresponding to obstacle proximity. The stimulus train at each frequency consisted of 10 spikes (B) 50 V (electronic-mode) / (C) 2V (ionotronic-mode). (D) Filter gain = A_{10}/A_1 plotted as a function of presynaptic spike frequency.

Activated by physical modalities like visible light, sound, heat, touch, etc. or by chemical signals such as smell and taste, sensory neurons transmit external stimuli information to the brain via interneurons. Here, we mimic sensory neural communication of the eye by integrating our artificial synapses with a photodetector [light dependent resistor (LDR)] via a microprocessing circuit (Figure S4-A). Here, the photodetector served as the dendritic input, arduino microcontroller acted as soma and our devices simulated the communication protocol between two sensory neurons. Variable response of resistance to light was utilized to detect obstacle proximity to portray a real-life application scenario with our artificial synapse. The processing circuit, connected to the gate terminal was programmed to fire spike trains of specific frequencies in response to obstacle proximity. Example: When an object was brought very close (< 2 cm) to the LDR, the resistance change dependent on the incident light intensity, was picked up by the processing circuit, which in turn triggered presynaptic spikes at a frequency of 45 Hz (amplitude = 50 V (electronic-mode)/ 2 V (ionotronic-mode)) to the presynaptic terminal of the TFT; inducing a post synaptic spike train response as shown in figure S4-B, C. High frequency activation enhanced the gain of all devices, with ionotronic-mode depicting a highest gain of 16.5 at 45 Hz, when compared to 1.86 for the electronic-mode (figure S4-D). The proximity stimulated post synaptic response presented here is simple and versatile, yet shows great potential and applicability for simulating various neural processes

Ebbinghaus Learning Curve: Learning rate in our artificial synapses were compared by recording EPSCs as a function of number of presynaptic spikes (Figure S5). The number of presynaptic spikes here, reflected the number of learning attempts and normalization with the peak value of post-synaptic response obtained from the largest number of rehearsals (100 in our case) reflected the differences in learning process in the compared systems. While electronic-mode operation depicted a steep increase in learning during the initial spikes, ionotronic-mode showed a slower but more flexible learning process in congruence with the learning model proposed by Ebbinghaus.[18] Assuming similar functionalities learnt with the two synapses, electronic-mode operation depicted the steepest slope and hence, fastest learning, followed by ionotronic-mode.

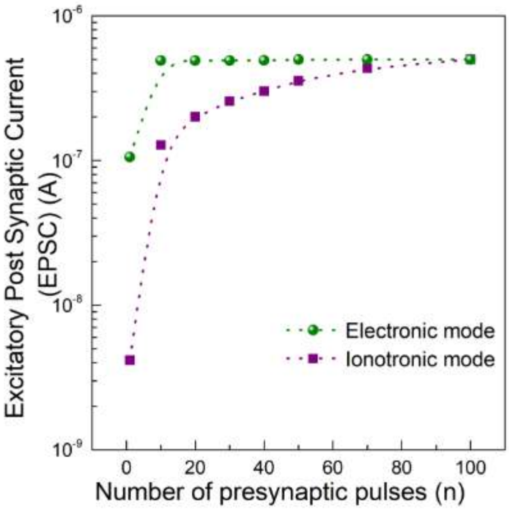

Figure S5. EPSC increment in response to increasing number of presynaptic pulses.

The learning curve exhibited by type-II TFTs could be defined by the equation:

$$y = y_0 + B_1 * \left(\exp\left(\frac{x}{t_1}\right)\right)$$

where x is number of presynaptic spikes with a constant pulse width of 22 ms, y_0 is the resting facilitation magnitude, B_1 *is* the initial facilitation magnitude of the learning phase, and t_1 *is* the characteristic learning time. The steepest slope in the initial stages represented fast progress in learning; whereas saturation at the latter stages indicated diminished progress after mastering the new knowledge. From the above graph, the total PSC could be seen in general as a function of the number of neurotransmitters (n) released per event of an action potential (V_{ap}) as per the quantal theory, i.e., $PSC \propto f(nV_{ap})$. The function here was dependent on the charge trapping possibilities depicted by both systems. While type-II systems depicted a slow initial increase, and fitted well with an exponential growth function, type-I TFTs quickly saturated within the first few rehearsals.

Note 5: Amplitude modulation with V_{ds} and pulse-width modulation with V_{gs}

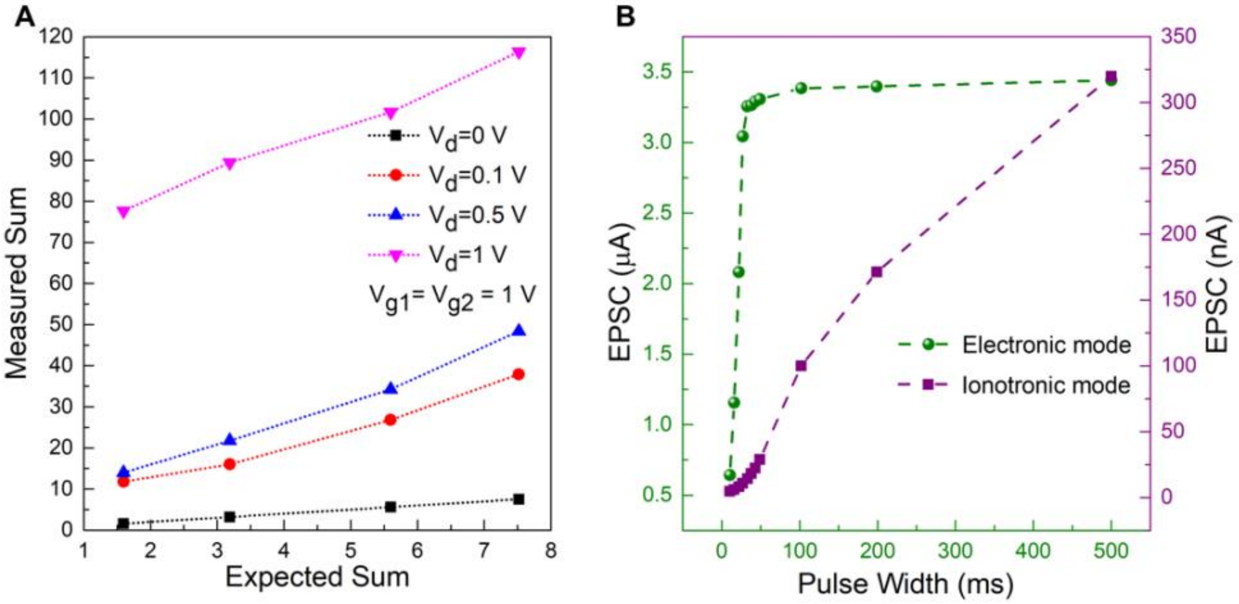

Figure S6. (**A**) Neuronal signalling modulations with rate coding schemes as a function of drain voltage V_d, (**B**) SDDP: EPSC modulation with presynaptic pulse width.

Non-Linear Integration: In contrast to earlier neuromorphic computational models, recent studies predict dendritic integration to be ubiquitously non-linear.[19] The effective sum of multiple inputs can be larger than their arithmetic sum (superlinear) due to the opening of voltage-gated channels; or smaller (sublinear) because of synaptic current saturation.[20] Such dendritic nonlinearities enhance neuronal processing capabilities at the single-neuron level. Here, superlinear amplification could be achieved by modulating the amplitude of source-drain voltage (V_d) as shown in figure S6-A. This additional control makes it possible to modulate the resistance states even further, making it possible to achieve complex processing functionalities with a simple circuit design. While changes in slope represented neuronal gain modulation, offset or x-axis intercept changes represented additive operation. Offset shift to the left represented excitation modulation with positive drain voltages, and right shift represented inhibition.[21,22]

Spike-duration dependent plasticity (SDDP): SDDP represents temporal causations between presynaptic action potentials. Here, SDDP was investigated as a function of increasing presynaptic pulse widths (Figure S6-B). EPSC amplitude increased from 642 nA to 3.4 μA (electronic-mode), 4.6 to 320 nA (ionotronic-mode), for spike durations ranging from 10 to 500 ms. While devices in electronic-mode saturated quickly within presynaptic pulse widths of 33 ms, ionotronic-mode operation depicted a linearly increasing trend in the measured range without signs of any saturation, similar to the trend with the number of rehearsals (Figure S5). The difference in time scales of saturation indicated differences in availability of mobile charges in the two systems under test. Understandably, trapping-detrapping of electrons occurred at much shorter timescales when compared to the slow ion induced electronic changes. The non-saturating behaviour of ionotronic-mode operation also indicated a larger reservoir of ions and charge carriers in the system. These differences could in turn be utilized to implement rate coded algorithms with concurrent multiple bit storage and processing capabilities. From SDDP, the probabilistic / stochastic nature of neurotransmitter release could be modelled by the equation, $PSC \propto p*f(nV_{ap})$, where the vesicular release probability "p" relied on the pulse width of the presynaptic spikes.

Note 6: Comparison with state-of-the-art

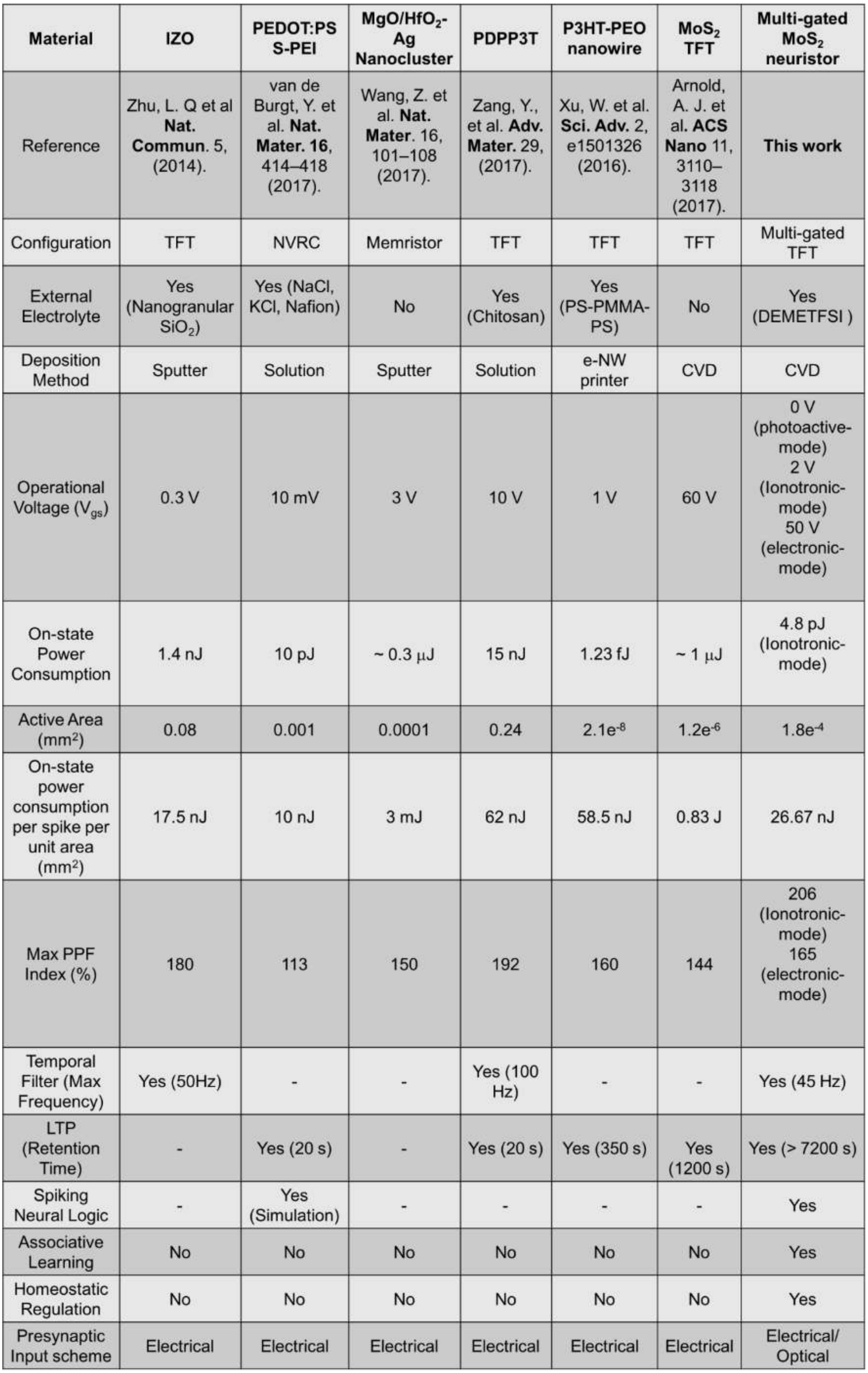

Material	IZO	PEDOT:PSS-PEI	MgO/HfO$_2$-Ag Nanocluster	PDPP3T	P3HT-PEO nanowire	MoS$_2$ TFT	Multi-gated MoS$_2$ neuristor
Reference	Zhu, L. Q et al **Nat. Commun**. 5, (2014).	van de Burgt, Y. et al. **Nat. Mater. 16**, 414–418 (2017).	Wang, Z. et al. **Nat. Mater**. 16, 101–108 (2017).	Zang, Y., et al. **Adv. Mater.** 29, (2017).	Xu, W. et al. **Sci. Adv.** 2, e1501326 (2016).	Arnold, A. J. et al. **ACS Nano** 11, 3110–3118 (2017).	**This work**
Configuration	TFT	NVRC	Memristor	TFT	TFT	TFT	Multi-gated TFT
External Electrolyte	Yes (Nanogranular SiO$_2$)	Yes (NaCl, KCl, Nafion)	No	Yes (Chitosan)	Yes (PS-PMMA-PS)	No	Yes (DEMETFSI)
Deposition Method	Sputter	Solution	Sputter	Solution	e-NW printer	CVD	CVD
Operational Voltage (V_{gs})	0.3 V	10 mV	3 V	10 V	1 V	60 V	0 V (photoactive-mode) 2 V (Ionotronic-mode) 50 V (electronic-mode)
On-state Power Consumption	1.4 nJ	10 pJ	~ 0.3 μJ	15 nJ	1.23 fJ	~ 1 μJ	4.8 pJ (Ionotronic-mode)
Active Area (mm^2)	0.08	0.001	0.0001	0.24	2.1e^{-8}	1.2e^{-6}	1.8e^{-4}
On-state power consumption per spike per unit area (mm^2)	17.5 nJ	10 nJ	3 mJ	62 nJ	58.5 nJ	0.83 J	26.67 nJ
Max PPF Index (%)	180	113	150	192	160	144	206 (Ionotronic-mode) 165 (electronic-mode)
Temporal Filter (Max Frequency)	Yes (50Hz)	-	-	Yes (100 Hz)	-	-	Yes (45 Hz)
LTP (Retention Time)	-	Yes (20 s)	-	Yes (20 s)	Yes (350 s)	Yes (1200 s)	Yes (> 7200 s)
Spiking Neural Logic	-	Yes (Simulation)	-	-	-	-	Yes
Associative Learning	No	No	No	No	No	No	Yes
Homeostatic Regulation	No	No	No	No	No	No	Yes
Presynaptic Input scheme	Electrical	Electrical	Electrical	Electrical	Electrical	Electrical	Electrical/ Optical

Table T2. Comparison with state of the art.

Note 7: Long-term plasticity

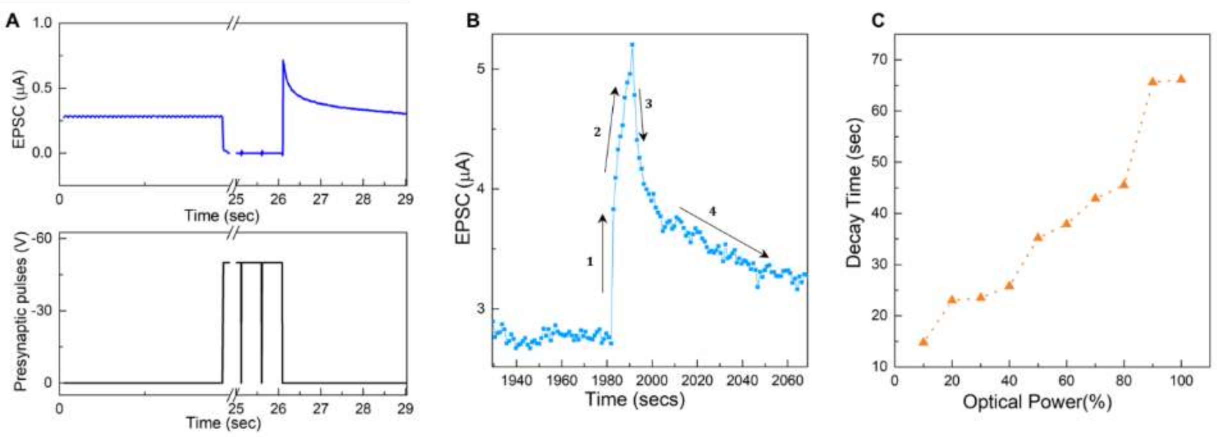

Figure S7. (**A**) Long-term potentiation (LTP) in electronic mode (**B**) Magnified view of the transient post synaptic conductance change on optical illumination (λ = 445 nm, 5.25 mW/mm^2). (**C**) Variation in decay / relaxation time as a function of the percentage of incident optical power.

Figure S7-A depicts the long-term potentiation (LTP) in electronic mode. For the photoactive-mode, we observed a light-induced change in the free carrier concentration which persisted after the optical excitation was removed, a phenomenon called Persistent photoconductivity (PPC) (Figure S7-B). The above figure shows a magnified view of the current response on excitation by a photon pulse (5.25 mW/mm^2, λ = 445 nm). The initial rapid increase in current was attributed to band-to-band transitions generating electrons and holes, while the subsequent slow increase deviated from this behaviour. The rapid decay following cessation of optical excitation could be attributed again band-to-band transitions. The following PPC was in congruence with the random local potential fluctuations (RLPF) model[23], with surface adsorbates, sulphur vacancies, etc. acting as possible sources for these trap states. We attribute this behaviour to intrinsic defects in at the MoS_2-SiO_2 interface since all measurements were conducted in high vacuum (10^{-7} mbar). As seen from figure 2C and S7-B, the device conductance was greatly enhanced and remained in a high-conductivity state for a period > 2 hours. Longer illumination power resulted in higher conductance and hence higher synaptic weight. Higher photo-dose also increased the decay lifetime as shown in figure S7-C. More carriers excited under higher photon doses could redistribute to occupy the sites of the local potential minima, resulting in a larger decay time after the photoexcitation was terminated.

This was again in good agreement with the RLPF mechanism.

Note 8: Input waveforms used to implement STDP protocol

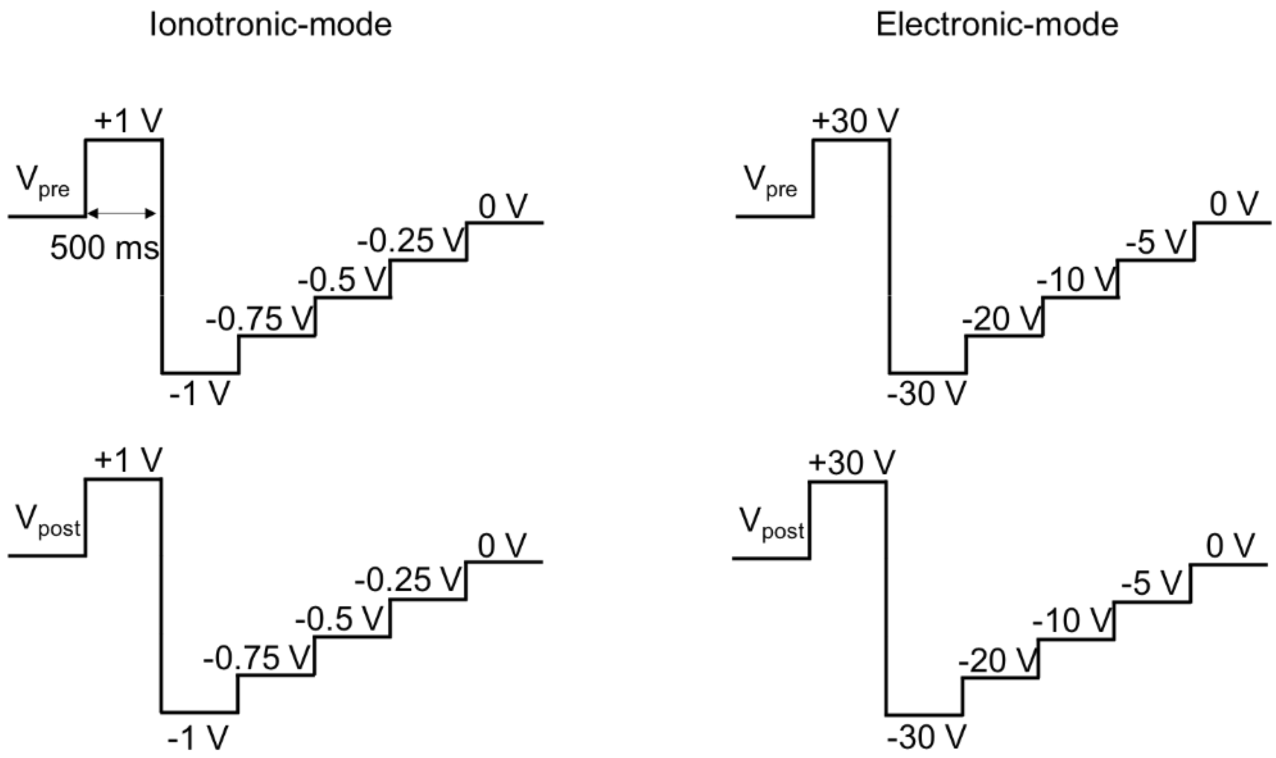
Ionotronic-mode
Electronic-mode
+1 V
Vpre
500 ms
0 V
-0.25 V
-0.5 V
-0.75 V
-1 V
+1 V
Vpost
0 V
-0.25 V
-0.5 V
-0.75 V
-1 V
+30 V
Vpre
0 V
-5 V
-10 V
-20 V
-30 V
+30 V
Vpost
0 V
-5 V
-10 V
-20 V
-30 V

Figure S8. Input waveforms used to generate STDP data in the ionotronic and electronic-modes respectively. The pulse width used for this measurement = 500 ms.

Note 9: Effective Association

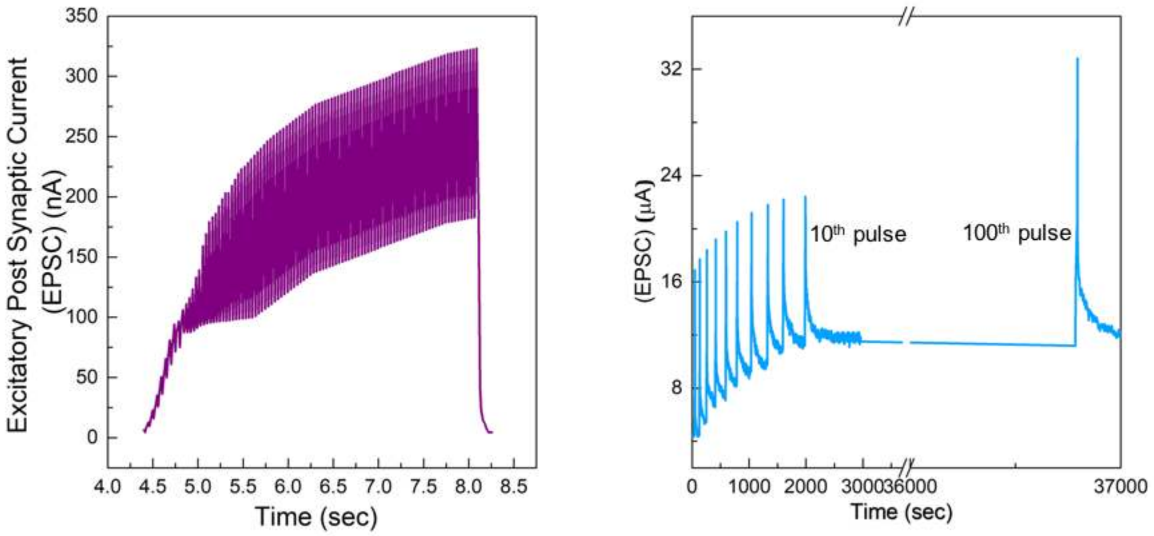

Figure S9. Output waveforms in response to persistent activation of action potentials (left) ionotronic-mode: 100 pulses with width = 22 ms was applied at the gate terminal and (right) 100 optical pulses of wavelength 445 nm, power = 5.25

mW/mm^2 and width = 10 s was applied to activate EPSCs. Comparison of the absolute values of EPSCs on individual and simultaneous application of electrical and optical stimuli reveals a super-linear increase in EPSCs to ~ 40 µA with simultaneous activation (>individual activation), reiterating the effective association achieved between the conditioned and unconditioned stimuli used in this study upon persistent training. This also reflects in the time taken for extinction of memory in our observation.

References:

[1] H. Li, Q. Zhang, C. C. R. Yap, B. K. Tay, T. H. T. Edwin, A. Olivier, D. Baillargeat, Adv. Funct. Mater. 2012, 22, 1385.

[2] K. F. Mak, C. Lee, J. Hone, J. Shan, T. F. Heinz, Phys. Rev. Lett. 2010, 105, 136805.

[3] M.-W. Lin, I. I. Kravchenko, J. Fowlkes, X. Li, A. A. Puretzky, C. M. Rouleau, D. B. Geohegan, K. Xiao, Nanotechnology 2016, 27, 165203.

[4] M. M. Perera, M.-W. Lin, H.-J. Chuang, B. P. Chamlagain, C. Wang, X. Tan, M. M.-C. Cheng, D. Tománek, Z. Zhou, ACS Nano 2013, 7, 4449.

[5] T. Li, G. Du, B. Zhang, Z. Zeng, Appl. Phys. Lett. 2014, 105, 93107.

[6] Y. Guo, X. Wei, J. Shu, B. Liu, J. Yin, C. Guan, Y. Han, S. Gao, Q. Chen, Appl. Phys. Lett. 2015, 106, 103109.

[7] Y. Park, H. W. Baac, J. Heo, G. Yoo, Appl. Phys. Lett. 2016, 108, 83102.

[8] J. Shu, G. Wu, Y. Guo, B. Liu, X. Wei, Q. Chen, Nanoscale 2016, 8, 3049.

[9] L. F. Abbott, S. B. Nelson, Nat. Neurosci. 2000, 3, 1178.

[10] D. Purves, G. J. Augustine, D. Fitzpatrick, L. C. Katz, A.-S. LaMantia, J. O. McNamara, S. M. Williams, Neuroscience, 2001.

[11] T. C. Sudhof, Annu. Rev. Neurosci. 2004, 27, 509.

[12] T. Branco, K. Staras, Nat. Rev. Neurosci. 2009, 10, 373.

[13] J. Del Castillo, B. Katz, J. Physiol. 1954, 124, 560.

[14] B. Katz, R. Miledi, J. Physiol. 1968, 195, 481.

[15] N. P. Vyleta, P. Jonas, Science (80-.). 2014, 343, 665.

[16] S. L. Jackman, J. Turecek, J. E. Belinsky, W. G. Regehr, Nature 2016, 529, 88.

[17] P. Feng, W. Xu, Y. Yang, X. Wan, Y. Shi, Q. Wan, J. Zhao, Z. Cui, Adv. Funct. Mater. 2016.

[18] J. M. J. Murre, J. Dros, PLoS One 2015, 10, e0120644.

[19] T. V Bliss, G. L. Collingridge, Nature 1993, 361, 31.

[20] A. Polsky, B. W. Mel, J. Schiller, Nat. Neurosci. 2004, 7, 621.

[21] F. S. Chance, L. F. Abbott, A. D. Reyes, Neuron 2002, 35, 773.

[22] E. Salinas, P. Thier, Neuron 2000, 27, 15.

[23] Y.-C. Wu, C.-H. Liu, S.-Y. Chen, F.-Y. Shih, P.-H. Ho, C.-W. Chen, C.-T. Liang, W.-H. Wang, Sci. Rep. 2015, 5.